J. Fluid Mech. (1994), *vol.* 269, *pp.* 199–246

Experimental and computational studies of mixing in complex Stokes flows: the vortex mixing flow and multicellular cavity flows

By SADHAN C. JANA†, GUY METCALFE AND J. M. OTTINO

Department of Chemical Engineering, Robert R. McCormick School of Engineering and Applied Science, Northwestern University, Evanston, IL 60208-3120, USA

(Received 20 May 1993 and in revised form 13 December 1993)

A complex Stokes flow has several cells, is subject to bifurcation, and its velocity field is, with rare exceptions, only available from numerical computations. We present experimental and computational studies of two new complex Stokes flows: a vortex mixing flow and multicell flows in slender cavities. We develop topological relations between the geometry of the flow domain and the family of physically realizable flows; we study bifurcations and symmetries, in particular to reveal how the forcing protocol's phase hides or reveals symmetries. Using a variety of dynamical tools, comparisons of boundary integral equation numerical computations to dye advection experiments are made throughout. Several findings challenge commonly accepted wisdom. For example, we show that higher-order periodic points can be more important than period-one points in establishing the advection template and extended regions of large stretching. We demonstrate also that a broad class of forcing functions produces the same qualitative mixing patterns. We experimentally verify the existence of potential mixing zones for adiabatic forcing and investigate the crossover from adiabatic to non-adiabatic behaviour. Finally, we use the entire array of tools to address an optimization problem for a complex flow. We conclude that none of the dynamical tools alone can successfully fulfil the role of a merit function; however, the collection of tools can be applied successively as a dynamical sieve to uncover a global optimum.

1. Introduction

The study of mixing by chaotic advection in Stokes flows has reached a certain level of maturity. By maturity we mean that several prototypical flows have been extensively studied – analytically, computationally, and experimentally – and that a few are thought of as well understood and have become emblematic of the general problem of chaotic advection (tables of examples are given in Ottino 1990 and Aref 1991). However, of the examples of prototypical Stokes flows only the eccentric cylinder flow and the cavity flow (Chaiken *et al.* 1986; Swanson & Ottino 1990; Leong & Ottino 1989*a*) have been the subject of simultaneous experimental and computational investigation. Not coincidentally, the eccentric cylinder flow has an analytical solution for the velocity field (Wannier 1950; Ballal & Rivlin 1976). Moreover, all of these systems are two-dimensional; only a handful of works have ventured into experiments involving three-dimensional flows (Kusch & Ottino 1992). Moreover, the cleanest

† Present address: The Benjamin Levich Institute, Steinman Hall, 1M, City University of New York, 140th Street & Convent Avenue, New York, NY 10031, USA.

applications pertain to two-dimensional and simple – as opposed to 'complex' – Stokes flows.

Streamline patterns in bounded flows consist only of closed recirculating cells and the streamlines that separate them. The separating streamlines may start and end at parabolic points on stationary surfaces or at hyperbolic points inside the fluid. We define a *primary cell* as a closed recirculation zone with some part of its bounding streamline in contact with at least one of the moving boundaries and a *secondary cell* as a closed recirculation zone with no part of its bounding streamline in contact with moving boundaries. *Complex Stokes flows* are then defined as those flows possessing secondary cells, i.e. flows where secondary cell motion is driven by contact with primary cells. So, for instance, drag flows in nearly square cavities are simple, while Moffatt's corner flows or the flow within slender cavities are complex (Chien, Rising & Ottino 1986; Leong & Ottino 1989*a*; Moffatt 1964; Jeffrey & Sherwood 1980; Jana & Ottino 1992).

There are two main objectives to this paper.

(i) *The presentation of new results for complex Stokes flows*

Here the focus is to define, develop, and analyse two examples of complex Stokes flows using a concerted combination of experiment and computation. A complex flow has several cells, is subject to bifurcation, and its velocity field is, with rare exceptions, only available from numerical computation. For steady flows we develop topological relations, study bifurcations and symmetries, and investigate how the forcing protocol's phase hides or reveals symmetries. To characterize mixing patterns we apply dynamical tools, such as Poincaré sections, Melnikov's method, periodic points and their manifolds, stretching along manifolds, and distributions of stretching throughout the flow. Comparisons of numerical computations to dye advection experiments are made throughout the paper.

(ii) *The critical evaluation of both old and new dynamical techniques*

Whereas the objective of (i) is self-evident, (ii) requires additional commentary. There has not been a thorough comparison, using the array of recently developed dynamical tools, between experiments and computation. The goal here is to consider many of these techniques applied to the analysis of chaotically advecting systems and extend them to the analysis of flows more general than simple flows with analytical solutions. The tools of analysis we will consider are the Melnikov method, Poincaré map, flow symmetries, periodic points, manifolds of hyperbolic periodic points, stretching distributions, dye advection experiments, and adiabatic methods. Passing comments are made regarding the use of mixing windows and stretching function distributions. Two questions arise. Given a diverse but incomplete body of techniques for the analysis of mixing systems, what is the best way to evaluate the known techniques so as to obtain a coherent structure for analysing general mixing flows? What kind of balance exists between the information obtained and the computational cost?

These issues have to do with efficient *extensibility* and meaningful *extrapolation*. New techniques developed and vetted on a single prototype flow may not readily generalize when extended to the analysis of new or more complex flows. In fact, much of the development of new techniques has been made easier by the fact that several prototypical flows have an exact closed form expression for the velocity field. In some cases this allows the derivation of fully analytical results. But more importantly, in all cases, this makes feasible numerical integrations to the accuracy required for chaotic advection studies. One reason for a particular tool's lack of extensibility may be that

it was developed on a flow with an analytically known velocity field: when $\boldsymbol{u}$ must be numerically obtained, a tool may become infeasible or unwieldy to use. When pushed into use for the analysis of new or more complex flows, it is not clear which techniques will remain appropriate and useful, and which ones will become in practice too difficult to apply. When no techniques exist to answer certain questions, rules of thumb often grow up to cover the gaps. The issue here is to decide what questions the existing analysis is able/unable to answer and to decide if meaningful extrapolation exists. In chaotic advection studies these rules of thumb have mostly to do with extrapolating local information to anticipate global trends, for instance that the best mixing comes from the manifolds associated with the lower-order periodic points with the largest eigenvalue, or extrapolating asymptotic results to anticipate short-time behaviour, for instance using Poincaré sections to anticipate the mixing results of a few periods. These extrapolations are made because some things are easily calculable and the implicit hope is that they will shed some light on those that are not readily calculable. From the application of incomplete analysis to only simple mathematical and experimental model flows, a 'common wisdom' grows up, most of it having to do with the global trends one might expect from only knowing local information. The question is to see if this wisdom is really at the level of rules of thumb, or whether it is often violated outside the simplest of flows.

In order to provide a common, versatile, and exacting testbed for tools and techniques, we have developed a new flow geometry, the vortex mixing flow (VMF) and have extended investigations in driven cavity flows to multicellular cavity flows (MCF). The geometry of the VMF consists of three coaxial cylinders, two of smaller diameter inside a third. The two inner cylinders rotate independently to drive the flow. The VMF may be thought of as a realization of the blinking vortex model (Aref 1984) or an idealization of the cross-sectional flow in a twin-screw extruder, in some sense an intermediate between a simple mathematical model flow and an industrially important application. The most important characteristics of the VMF are that it easily produces a variety of complex Stokes flows, it has no analytical solution for the velocity field, and it is a relatively easy experiment to build and operate.

The variety of different complex flows is a consequence of the existence of flow bifurcations. Many parameters are available to tune the flow, several of which are cylinder placement and shape, relative cylinder size, and rotation speed. This defines a multiparameter bifurcation problem and the many different complex Stokes flows unfold from the many solution branches of the bifurcation problem. Here we will restrict ourselves to varying only two parameters: a geometric parameter governing cylinder placement, and a forcing parameter governing the speed ratio of the inner cylinders. In the case of the MCF the parameter space consists of the aspect ratio of the cavity and the speed ratio of the walls; this system yields a more compact presentation of bifurcation results.

We finish our assessment of dynamical tools in § 7 by posing a complex test problem. The problem is to find the optimum mixing configuration for the VMF. A fairly complete characterization of the state of mixing is provided by the stretching distribution and our initial efforts were to determine if this or any of the other tools could fill the role of the merit function of traditional optimization. We find, however, that no single existing dynamical characterization satisfactorily fulfils this role. However, the collection of tools can be applied successively as a 'sieve' to remove most of the parameter space and uncover an approximation to a global optimum.

The rest of the paper is arranged as follows. The geometry of the example flows, along with numerical solutions using boundary integral equation methods and a

description of the experimental set-up, is presented in §2. Section 3 focuses on the piecewise-steady flows that force chaotic advection, specifically topological invariance relations, flow bifurcations, and symmetry considerations. Section 4 focuses on the dynamical tools: Poincaré sections, short-time dye advection experiments, periodic points, manifolds of hyperbolic periodic points, stretching, and the Melnikov method. In §5 we establish, using three methods, that the dye advection patterns in chaotic flows are qualitatively independent of the specific waveform of the boundary motion forcing for a broad class of waveforms. Section 6 focuses on the advection characteristics of dynamical systems with slowly varying parameters and the crossover from adiabatic to non-adiabatic behaviour. Section 7 contains the test problem and §8 summarizes the uses and limitations of the dynamical tools and prioritizes the available tools for use in analysing a new mixing flow.

2. Flow systems

2.1. *Geometries and parameters*

Figure 1 (*a*) shows the VMF geometry. An outer cylinder of radius R_o houses two inner cylinders of equal radii R_i. Fluid fills the space between the inner and outer cylinders. The centres of the inner cylinders lie along a diameter of the outer cylinder and are set symmetrically about the centre. The ratio R_o/R_i for this paper is fixed at 4. Inner-cylinder placement characterizes the remaining family of geometries and is parametrized by the cylinder eccentricity

$$e = d/(R_o - R_i), \tag{1}$$

where d is the distance between the centres of the outer and inner cylinders. The inner and outer cylinders rotate in place to force the flow. If Ω_o, Ω_A, and Ω_B are the angular velocities of respectively the outer cylinder and inner cylinders and ν is the kinematic viscosity of the fluid, then

$$Re = [\Omega_o^2 R_o^2 + (\Omega_A^2 + \Omega_B^2) R_i^2]^{\frac{1}{2}} (R_o - R_i)/\nu \tag{2}$$

defines the Reynolds number. When the outer cylinder is stationary, the speed ratio of the inner cylinders of the VMF,

$$r = \Omega_A/\Omega_B, \tag{3}$$

which may be positive or negative for co- or counter-rotating motion, characterizes the forcing. The Strouhal number is

$$St = \frac{R_o - R_i}{[\Omega_o^2 R_o^2 + (\Omega_A^2 + \Omega_B^2) R_i^2]^{\frac{1}{2}} T}, \tag{4}$$

where T is the period of the flow.

Figure 1 (*b*) shows the MCF geometry. A rectangular box of height H and width W has fluid inside. The sidewalls are stationary and the top and bottom walls move tangentially with velocities U_A and U_B respectively. The MCF has only two parameters available to tune the steady-state flows. These are the aspect ratio

$$A = W/H \tag{5}$$

and the speed ratio

$$r = U_A/U_B. \tag{6}$$

The Reynolds number for the MCF is

$$Re = \frac{(U_A^2 + U_B^2)^{\frac{1}{2}} H}{A\nu} \tag{7}$$

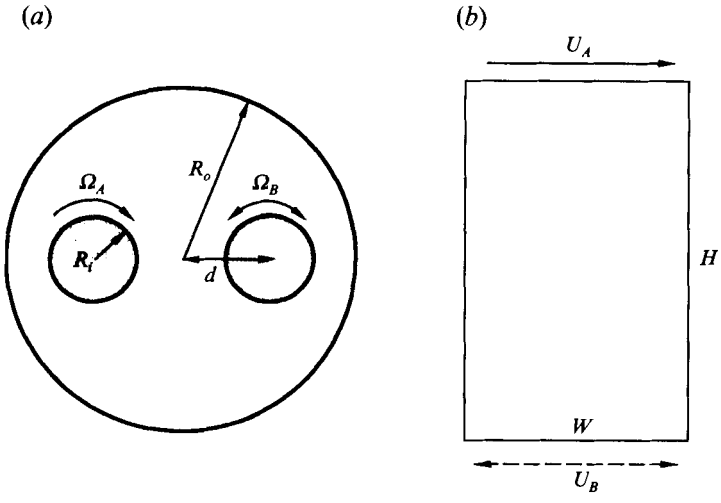

FIGURE 1. Geometries and definitions for the example flows: (*a*) vortex mixing flow, (*b*) slender cavity flow.

and the Strouhal number is

$$St = \frac{H^2/W}{T(U_A^2 + U_B^2)^{\frac{1}{2}}}. \tag{8}$$

Leong & Ottino (1989*a*) studied a similar flow with $A > 1$, for which one primary cell fills the cavity, and Leong (1990) presented a few results for slender flows. For $A < 1$ a series of cells fills the cavity, the exact number depending on A and weakly on r.

2.2. *Numerical evaluation of velocity fields*

None of the flows presented above has analytical solutions. Numerical solutions are sought using the boundary integral equation methods (BIEM) (Higdon 1985; Pozrikidis 1992) for the VMF and the finite difference method (Burggraf 1966; Pan & Acrivos 1965) for the MCF. The numerical integration of chaotic particle trajectories requires very accurate velocities. In fact, comparing calculated advection patterns to experiment, or comparing particle trajectories obtained from a numerical velocity field with an available analytical velocity field are stringent tests for numerically obtained velocity fields: small changes in the velocity field give rise to very different advection patterns. Recent calculations in our laboratory have shown that for Stokes flows in complicated domains sufficiently accurate velocity fields can be obtained using BIEM. Finite difference calculations are also reported by Leong (1990) and Ling & Schmidt (1991). As the BIEM may be somewhat less familiar, we present a brief description in Appendix A.

2.3. *Experiments*

The experimental apparatus used to produce the vortex mixing flow is a version of the eccentric cylinder apparatus of Swanson & Ottino (1990), modified by the addition of an independently driven second inner cylinder; a diagram is shown in figure 2. The inner diameter of the outer cylinder is 15.24 cm and the outer diameter of the inner cylinders is 3.81 cm. The arms holding the inner cylinders also mount motors (Bodine NSH-11D5), pulleys, and drive belts. The arms are designed for easy placement of the inner cylinders in order to obtain different eccentricities. Accurate cylinder placement is achieved by use of template covers of the outer cylinder, leading to an accuracy in

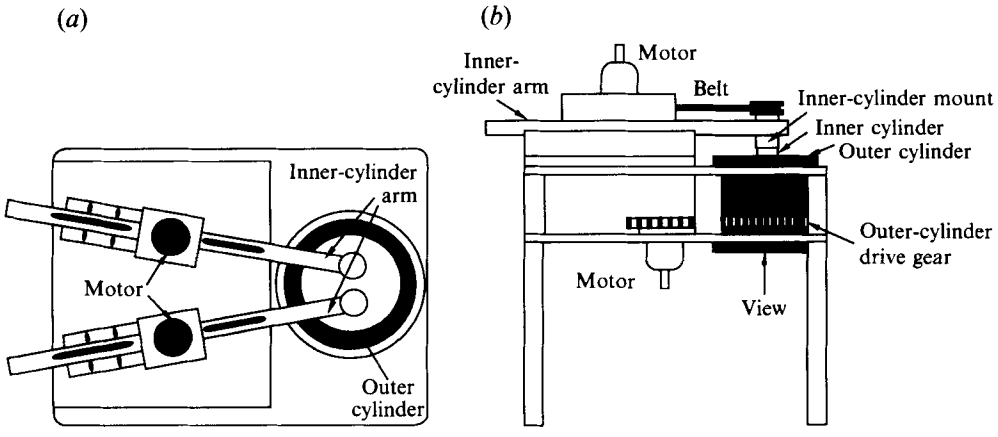

FIGURE 2. Schematic of the vortex mixing flow apparatus: (*a*) top view, (*b*) front view.

e of 0.05%. The cylinder motion is computer controlled using Keithly System 570 Data Acquisition software. Motors are calibrated before experiment runs and rotation is accurate to about 1°; speeds are accurate to 1%. The control schemes used in this work are similar to those in Swanson & Ottino (1990). In the VMF the left inner cylinder always rotates in the clockwise direction and the right inner cylinder rotates either clockwise or counterclockwise to produce respectively co- and counter-rotating motion. The apparatus used to produce the multicell cavity flow is described in Leong & Ottino (1989*a*). Motors and the control scheme are similar to those of the VMF. In the MCF the top wall always moves from left to right and the bottom wall moves either right to left or left to right to produce respectively co- and counter-rotating motion.

The fluid used in all experiments is glycerin (Emery 916 Glycerin 99.7%) with a viscosity $\sim$ 7 P and density 1.2 g cm^{-3}. The inner cylinder rotation speeds are 0.03–0.07 rev s^{-1}, giving a Reynolds number range of 0.08–0.2 and a Strouhal number range of 0.02–0.3. Fluid fills the outer VMF cylinder to a depth of 10 cm with a 2–3 cm layer of Fomblin® Y-L VAC 06/6 (perfluoropolyether vacuum-pump oil, Aldrich Chemical Company) at the bottom to eliminate bottom effects. For flow visualization a neutrally buoyant solution of fluorescent dye (Cole-Parmer, type 295-15, 295-17) in glycerin is used. The dye is illuminated from above with UV lights (long range, Spectronix XX-40) and other light sources are removed. Blobs of dye are injected 0.5–1 cm below the upper surface to obtain maximum illumination and avoid free-surface effects. The mixing patterns are photographed through the glass bottom of the outer cylinder with a Nikon 2004 camera, Nikkor micro f/4.0 105 mm lens, and Kodak Ektachrome 100 HC colour slide film. For convenience the photographs are taken through a mirror angled at 45° to the cylinder bottom.

3. Piecewise-steady flows

The simplest way to force time dependence in a Stokes flow is to alternate between a sequence of steady flows with different streamline patterns. Streamline crossing – superposed patterns showing non-tangential intersections – is a necessary and sufficient condition for generating chaos (see §4.4). Thus, when presented with a new complex flow, the initial investigation should focus on finding the possible steady streamline patterns. Once the steady flows are in hand, it is possible to predict streamline crossings, assess which flows will mix and, quite possibly, be able to infer

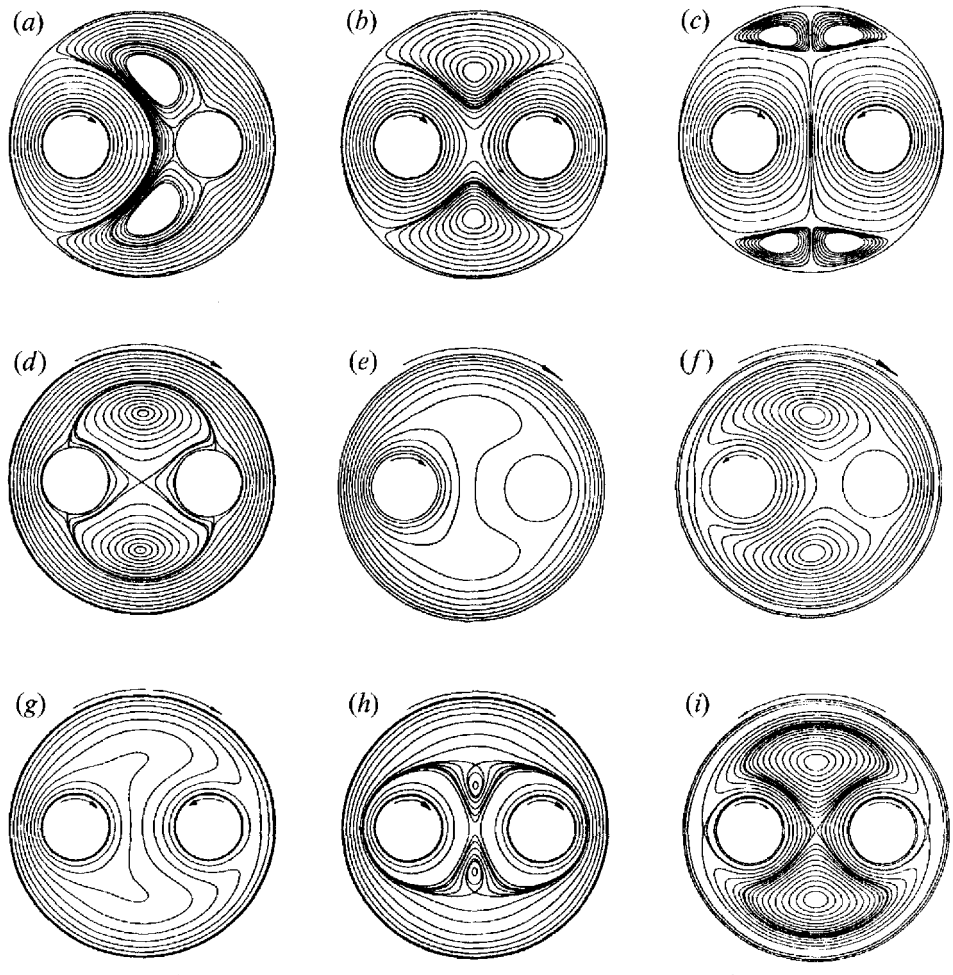

FIGURE 3. A set of nine possible streamline portraits of the vortex mixing flow. $R_o/R_i = 4$, $e = 0.67$. (*a*) $\Omega_A = 1$, $\Omega_B = 0$, $\Omega_o = 0$; (*b*) $\Omega_A = 1$, $\Omega_B = 1$, $\Omega_o = 0$; (*c*) $\Omega_A = 1$, $\Omega_B = -1$, $\Omega_o = 0$; (*d*) $\Omega_A = 0$, $\Omega_B = 0$, $\Omega_o = 1$; (*e*) $\Omega_A = 1$, $\Omega_B = 0$, $\Omega_o = 1$; (*f*) $\Omega_A = -1$, $\Omega_B = 0$, $\Omega_o = 1$; (*g*) $\Omega_A = 1$, $\Omega_B = -1$, $\Omega_o = 1$; (*h*) $\Omega_A = 1$, $\Omega_B = 1$, $\Omega_o = 1$; (*i*) $\Omega_A = 1$, $\Omega_B = 1$, $\Omega_o = -1$.

the extent of the mixing regions as well. The steady flows are arranged in sequences known as protocols, but in complex Stokes flows flow bifurcations are possible and even a simple protocol may involve many topologically different flows. The available flows are the physically realizable steady streamline patterns and the symmetry transformations of these patterns. The symmetries of the protocols are the symmetries of the chaotic flows as well. This fact can be exploited to reduce the computational burden of many of the dynamical tools considered in §4. Therefore, any chaotic advection study begins with a study of steady flows. In this section we begin by showing a topological result that allows us to infer almost all families of physically realizable steady flows for a given geometry. Then we show representative sequences of flow bifurcations, and finally discuss how the specific choice of periodic protocol affects flow symmetries.

3.1. *Critical points and flow topology*

Complex Stokes flows can produce a rich array of topologies. Representative sets of streamline portraits for the VMF are shown in figure 3 and for the MCF in figure 4.

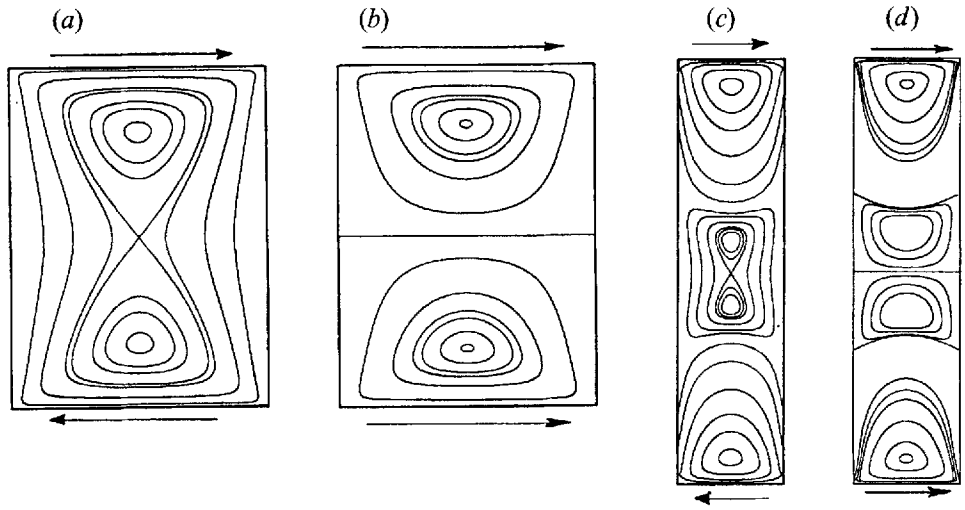

FIGURE 4. Typical streamline portraits of the cavity flows: (a) $A = 0.75$, $r = -1$; (b) $A = 0.75$, $r = 1$; (c) $A = 0.25$, $r = -1$; (d) $A = 0.25$, $r = 1$.

An array of *cellular* flows is possible depending upon the eccentricity or aspect ratio of the system and the velocity ratio of the walls or cylinders. For the VMF for fixed geometry and $|\Omega_K| = 0$ or 1, where $K = o$ (outer cylinder), A, or B, it is possible to show by symmetry arguments that there are only nine combinations of boundary motions that produce topologically distinct non-trivial patterns. Figure 3 shows such a set of patterns. For the MCF the only bifurcation is to add or subtract one cell (we do not consider corner Moffatt cells because of their small size). The recirculating regions in these flows arise either due to flow separation from stationary walls or due to the formation of separatrix streamlines within the fluid. The points of flow separation or reattachment and the points from which streamlines in the form of separatrices emanate are the critical points of the flow and require special attention. Elliptic and hyperbolic critical points occur inside the fluid. Fluid elements experience rotational motion about an elliptic point but stretch and compress about a hyperbolic point. Parabolic critical points occur on the stationary surfaces and for bounded flows always appear in pairs where they are commonly known as the flow separation and reattachment points. Apart from vanishing velocity, the vorticity also vanishes at parabolic points.

The flow pattern in Stokes flows is uniquely determined by geometrical parameters, e.g. eccentricity, aspect ratio, ratio of radii, etc., and boundary conditions, e.g. the instantaneous velocity ratio of the tangentially moving boundaries. Even after specifying these parameters, however, it is difficult to qualitatively predict the correct streamline pattern without resorting to the expense of exact computation. To partially address this difficulty it is useful to derive relations that allow, knowing only information along the boundary, predictions of the interior pattern.

Some topological ideas are useful in this regard. The *Poincaré index* of a critical point is obtained by travelling counterclockwise once around the point in a circular path and counting the number of counterclockwise revolutions made by a vector with its base on the path and its head always pointing in the direction of the flow. The Poincaré index of a hyperbolic point is -1, of an elliptic point is 1, and of a parabolic point is $-\frac{1}{2}$. The *Euler number* ξ of a surface is defined as the sum of the Poincaré indices of the critical points on the surface. An n-fold torus is said to have *genus n*. The

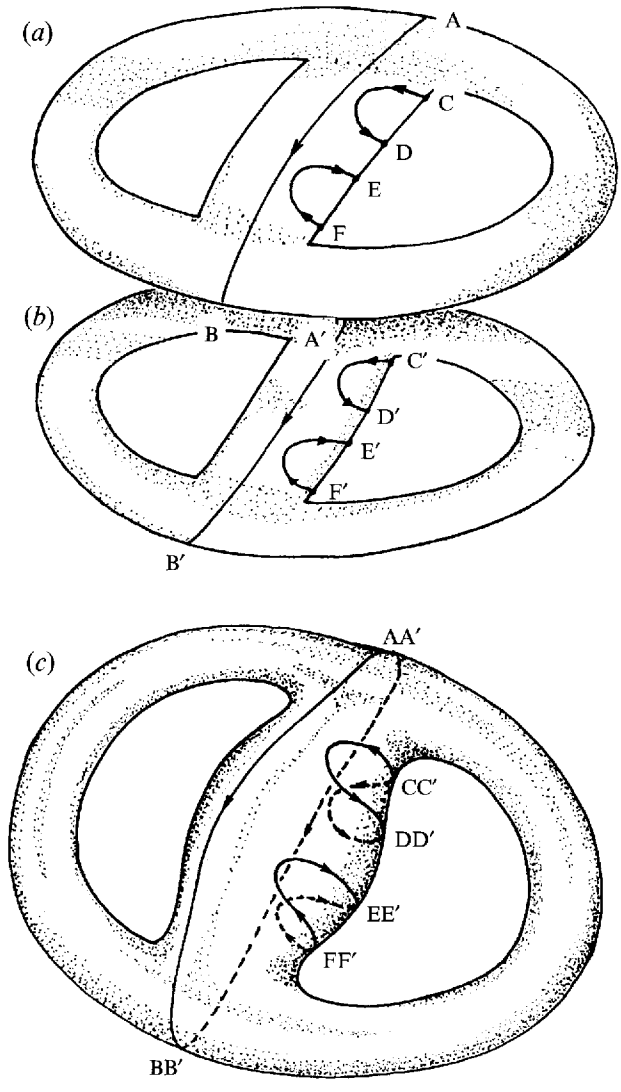

FIGURE 5. Sketch of vortex mixing flow on the surface of a two-fold torus: (*a*) represents the flow of figure 3(*a*) and the points A, B, C, D, E and F represent the parabolic points on the stationary walls; (*b*) is the image of (*a*) which together with (*a*) constitutes the flow on the surface of a two-fold torus, (*c*).

genus of a sphere is 0, of a one-fold torus is 1, of a two-fold torus is 2, and so on. Consider now the area-preserving flows on a surface of genus n. The Poincaré index theorem states that the Euler number and genus are related b y $\xi = 2-2n$ (Flegg 1974). The key step in applying these topological results to fluid flows is to convert the flow domain into an n-fold torus. We observe that the phase space of the VMF is topologically equivalent to one half of a two-fold torus in that the top half of the three-dimensional surface of the two-fold torus can be flattened and deformed into the VMF domain (see figure 5 and keep in mind that the critical points must be counted twice to account for the backside of the torus). Thus the Euler number of the VMF is -1 and the topological invariance relation for the VMF is

$$N_E-(N_H+\tfrac{1}{2}N_P) = -1, \tag{9}$$

where N_E is the number of elliptic points, N_H is the number of hyperbolic points, and

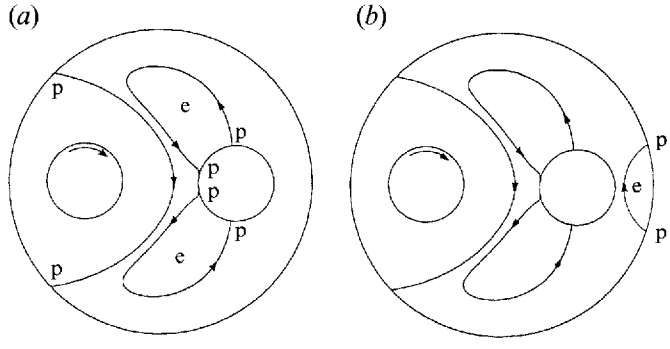

FIGURE 6. Possible separation patterns for the vortex mixing flow; e denotes the location of an elliptic point and p the location of a parabolic point; $R_o/R_i = 4$, $\Omega_A = 1$, $\Omega_B = 0$, $\Omega_o = 0$: (*a*) pattern determined via computation, (*b*) pattern ruled out by computation.

N_P is the number of parabolic points. By similar arguments two cavity flow patterns can be drawn on the surface of a regular octahedron which is topologically equivalent to a sphere. Thus the companion relation for cavities is

$$N_E - (N_H + \tfrac{1}{2}N_P) = +1. \tag{10}$$

An examination of all the streamline portraits in this paper (figures 3, 4, 7–9) verifies adherence to these invariance relations.

Topology aids in classifying flows with a rich bifurcation structure. A typical bifurcation sequence in the VMF on varying only one parameter might involve a dozen distinct streamline patterns (as opposed to a flow in an essentially infinite domain that has rather simple structures (Ng 1989)). As we show below, these complex Stokes flows have many distinct patterns that need some scheme to classify them. Even though one may use relations (9) and (10) to restrict consideration to realizable families of flows, topology alone cannot of course uniquely determine the flow pattern. For instance figure 6 shows candidate patterns for the VMF with one inner cylinder in motion. Figures 6(*a*) and 6(*b*) both satisfy (9). The easiest numerical check, without computing the entire streamline portrait, is to calculate the shear stress on the outer cylinder and then count the number of times the shear stress changes sign. The check in this case reveals two sign changes corresponding to two parabolic points on the outer cylinder, confirming figure 6(*a*) as the real flow.

3.2. *Flow bifurcations*

Both the VMF and MCF exhibit a rich flow bifurcation structure as their geometry and forcing parameters are varied. Obviously the mixing behaviour depends very strongly on the flow's position in the bifurcation diagram. Representative examples of VMF bifurcations are presented in figures 7–9. The flow patterns in figure 7 are obtained when only one inner cylinder is in motion and the eccentricity varies. Figure 8 is obtained when the inner cylinders move at equal speeds in the same direction and the eccentricity varies. Figure 9 is obtained with fixed eccentricity and varying the speed ratio of the inner cylinders. Many other bifurcations occur for other parameters, e.g. outer-cylinder motion, counter-rotating inner cylinders, or variation of the ratio of radii; however, these are not presented here. MCF bifurcations add a new secondary cell as the cavity becomes more and more slender (aspect ratio A becoming smaller). This is considerably simpler than the pattern changes in the VMF and so the results for the MCF can be presented in explicit bifurcation diagrams (figure 10) showing the

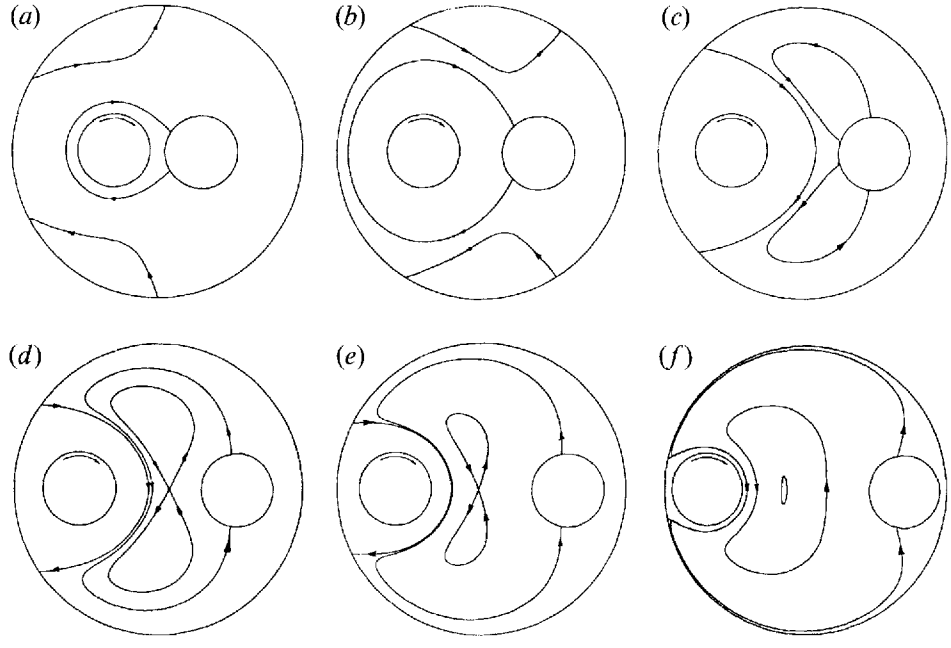

FIGURE 7. Flow separation patterns as a function of eccentricity for the vortex mixing flow with one cylinder rotating, $R_o/R_i = 4$: (*a*) $e = 0.40$, (*b*) $e = 0.53$, (*c*) $e = 0.67$, (*d*) $e = 0.76$, (*e*) $e = 0.80$, (*f*) $e = 0.93$.

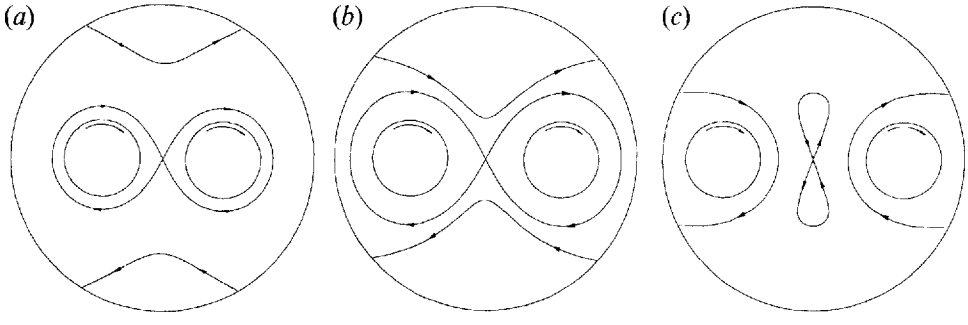

FIGURE 8. Flow separation patterns as a function of eccentricity for the vortex mixing flow with corotating inner cylinders; $R_o/R_i = 4$, $\Omega_A = 1$, $\Omega_B = 1$: (*a*) $e = 0.53$, (*b*) $e = 0.67$, (*c*) $e = 0.80$. Flow bifurcation between patterns (*b*) and (*c*) occurs at $e = 0.7045$.

number of cells as a function of the velocity ratio of the walls and aspect ratio of the cavity. (Corner or Moffatt cells are negligibly small compared to the size of the cavity and are not counted in figure 10.) Since the diagram is symmetric with respect to unity velocity ratio, only half the bifurcation diagram is shown in figure 10.

3.3. *Time-periodic protocols and symmetries*

Once the steady-state flows are known, the simplest way to generate time dependence in the velocity field and hence chaotic motion is by piecing together steady flows in time-periodic sequences known as protocols. Suitable periodic motions of the boundaries of the flow domain generate time-periodic flows. The generic form of boundary velocities is

$$u_A = U_A(1+\epsilon_A f_A(t)), \quad u_B = U_B(1-\epsilon_B f_B(t)), \tag{11a,b}$$

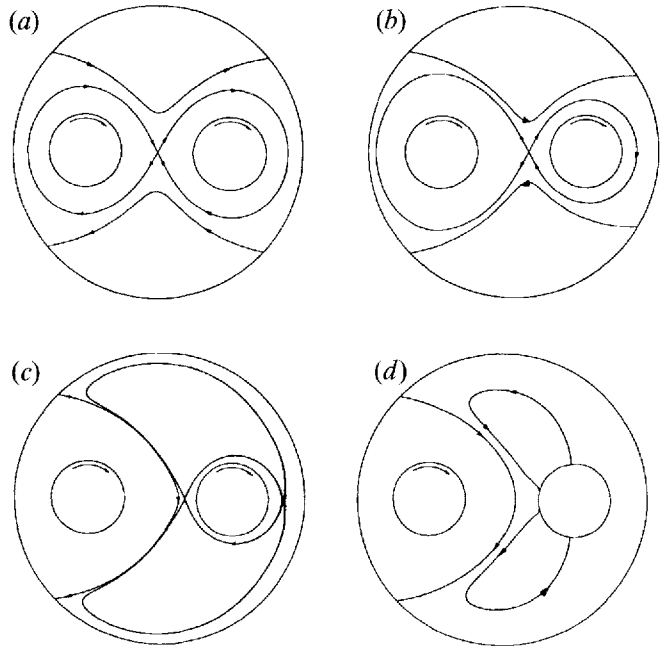

FIGURE 9. Flow separation patterns as a function of the speed ratio with corotating inner cylinders; $R_o/R_i = 4$, $e = 0.67$: (a) $r = 1$, (b) $r = 5$, (c) $r = 20$, (d) $r = \infty$, ($\Omega_A = 1$, $\Omega_B = 0$).

where u_A is the linear or angular velocity of the moving element A with mean velocity U_A, and similarly for u_B. The perturbation parameters $\epsilon_{A,B}$ determine the degree to which each boundary deviates from the mean velocities and $f_{A,B}(t)$ are the specific waveforms of the boundary motion. It is common to use a symmetric form of (11) and set $U_A = U_B = U$, $\epsilon_A = \epsilon_B = \epsilon$, and $f_A = f_B = f(t)$. Equations (11) fix the relative phase of the boundary motions at π. If $\epsilon = 0$, the boundaries move with constant velocities and the fluid particles follow regular trajectories: there is no chaos. The perturbation parameter ϵ determines the degree of chaos. One should especially note that in mixing studies the perturbation from integrability ϵ need not be small and in most cases is in fact quite large. Almost all studies take $f(t)$ to be a single-frequency undulatory motion, such as a square wave, sine wave, or sawtooth wave with the boundaries either co- or counter-rotating, although there is one theoretical study that considers quasi-periodic forcing (Beige, Leonard & Wiggins 1991).

Once the degree of deviation from integrability ($\epsilon > 0$) is set, it is common to parameterize the nonlinearity by the angular or linear boundary displacement per period, which is proportional to the energy input to the system per period. Protocols are usually arranged so that each motion imparts an equal 'amount of energy', i.e. linear displacements are made equal. The angular displacement per period of the inner cylinders in the VMF is

$$\theta = \int_0^T \Omega(t)\,\mathrm{d}t, \tag{12}$$

where T is the period of the boundary motion; the linear displacement per period of the top and bottom walls in the MCF is

$$D = \frac{1}{W}\int_0^T U\,\mathrm{d}t. \tag{13}$$

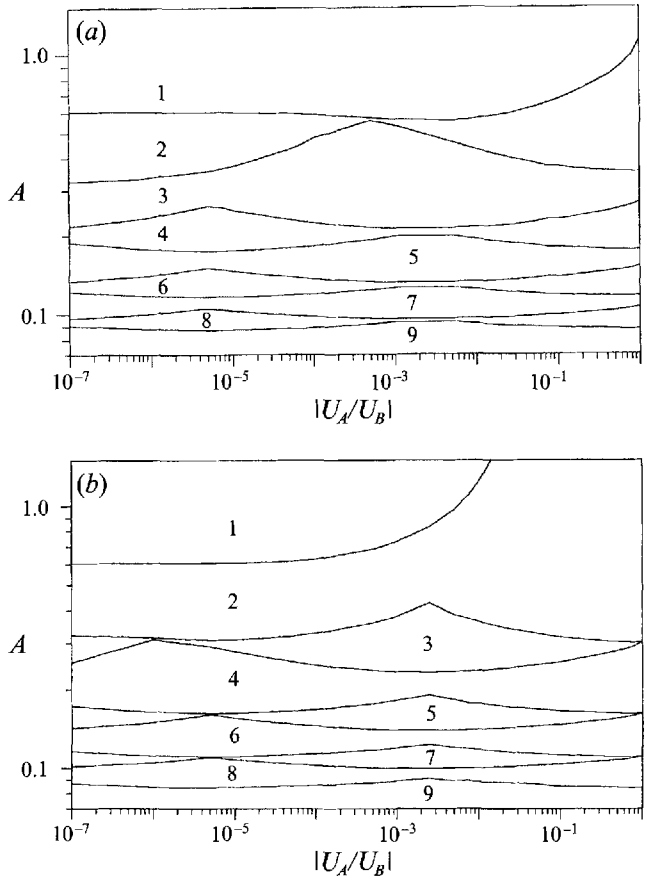

FIGURE 10. Bifurcation diagrams for a slender rectangular cavity flow. Numbers denote the number of primary cells. (*a*) Top and bottom walls move in opposite directions, (*b*) top and bottom walls move in the same direction.

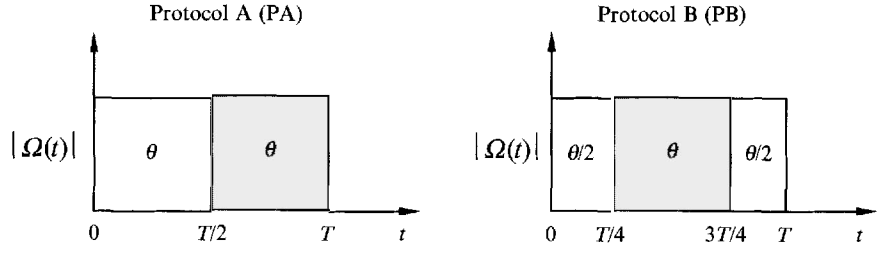

FIGURE 11. Time-periodic square-wave protocols. For the vortex mixing flow in protocol A each of the inner cylinders rotates alternatively through an angle θ starting with the left inner cylinder. In protocol B the left inner cylinder rotates through an angle $\theta/2$ both before and after the right inner cylinder rotates through θ. The plain rectangles describe the motion of the left inner cylinder and the shaded rectangles describe the motion of the right inner cylinder. For the cavity flow, the angle θ is replaced by the displacement D defined in (13) and the top wall moves first.

Mixing protocols dictate the symmetries of the flow. Figure 11 shows two particular square-wave protocols that will be used in the rest of the paper. In protocol A (PA) each of the moving elements accomplishes full displacement without interruption; in protocol B (PB) the first moving element describes its displacement per period in two

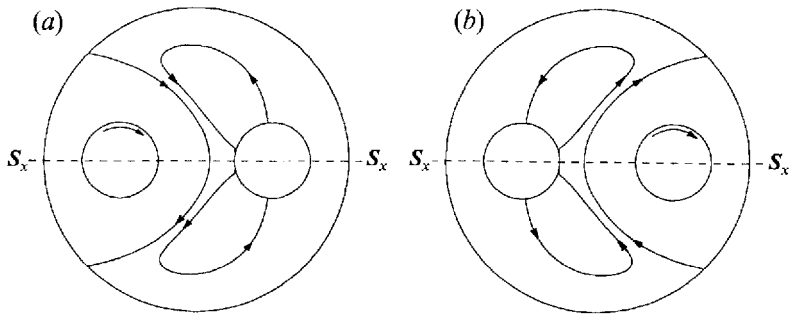

FIGURE 12. Symmetries of the component flows: (*a*) F_A, produced by the rotation of the left inner cylinder; (*b*) F_B, produced by the rotation of the right inner cylinder; $R_o/R_i = 4$, $e = 0.67$. Flow F_A can be obtained from F_B^{-1} by reflection on the y-axis.

stages. The only difference between PA and PB is the shift of the overall phase by $\frac{1}{4}$ period, but the overall phase has a subtle effect on the symmetries of the flow. Other waveform effects are discussed in detail in §5.

Symmetries of flows have been proved beneficial in many studies involving chaotic advection (Franjione, Leong & Ottino 1989; Franjione & Ottino 1992). Two flows $F_A(\cdot)$ and $F_B(\cdot)$ are *symmetric* to each other if there exists a transformation S such that

$$F_B(\cdot) = SF_AS^{-1}(\cdot). \tag{14}$$

If $F_B(\cdot) = F_A(\cdot)$ the flow is said to have *ordinary* symmetry; if $F_B(\cdot) = F_A^{-1}(\cdot)$ the flow possesses *time-reversal* symmetry. The transformation S can be as simple as reflection across the axes or rotation about the origin in a Cartesian frame. The reflectional symmetry across the x-axis is denoted by S_x, i.e. $(x, y) \rightarrow (x, -y)$; similarly, S_y denotes $(x, y) \rightarrow (-x, y)$. A 90° clockwise rotation is denoted by R which maps (x, y) into $(-y, x)$ and R^2, a rotation by 180°, corresponds to $(x, y) \rightarrow (-x, -y)$. It can be easily seen that $S_xS_x = 1$, $S_yS_y = 1$, $R^4 = 1$, and $R^2 = S_xS_y = S_yS_x$. The symmetry S is said to be orientation preserving if the determinant of the Jacobian is $+1$ and orientation reversing if the determinant is -1. The *fixed line* of the symmetry S is defined as a set of points $\{x\}$ that is invariant upon transformation, i.e. $S\{x\} = \{x\}$. Thus, for example, $S_y\{y\text{-axis}\} = \{y\text{-axis}\}$.

Consider the flows produced by the action of moving boundary A as $F_A(\cdot)$ and boundary B as $F_B(\cdot)$, e.g. in the VMF $F_A(\cdot)$ and $F_B(\cdot)$ could be left and right-cylinder motions, or in the MCF they could be motions of the top and bottom walls. It is apparent that $F_A(\cdot)$ and $F_B(\cdot)$ need not be restricted to only single boundary motions. For instance if we choose to compose the flows in figures 3(*a*) and 3(*c*) to make a protocol, then $F_B(\cdot)$ would have two boundaries in motion. The square-wave time-periodic flow in PA is produced by repeating the sequence $F_BF_A(\cdot)$; PB, corresponds to $F_A^{\frac{1}{2}}F_BF_A^{\frac{1}{2}}(\cdot)$. The index $\frac{1}{2}$ in flow $F_A^{\frac{1}{2}}(\cdot)$ means that the flow moves only half of its total displacement per period.

Both the cavity flow and the vortex mixing flow are doubly symmetric, i.e. they exhibit two independent symmetries. Two symmetries S_1 and S_2 are said to be independent if $S_1 \neq SS_2S^{-1}$ for all S. Figure 12 shows the streamline portraits of the component flows $F_A(\cdot)$ and $F_B(\cdot)$ of the VMF with a square-wave protocol consisting of one cylinder rotating, then its reflection. Each of the component flows has a reflectional symmetry across the x-axis (see table 1). In table 2, various symmetries of the time-periodic vortex mixing flows with PA and PB are presented. Similar relations can be easily derived for the cavity flows. The vortex mixing flow $F_BF_A(\cdot)$ with

	Flow A, F_A		Flow B, F_B	
Flow system	Self-symmetry	Relation to F_B	Self-symmetry	Relation to F_A
Cavity flow	$S_y F_A^{-1} S_y$	$S_x F_B^{-1} S_x$	$S_y F_B^{-1} S_y$	$S_x F_A^{-1} S_x$
Vortex mixing flow	$S_x F_A^{-1} S_x$	$S_y F_B^{-1} S_y$	$S_x F_B^{-1} S_x$	$S_y F_A^{-1} S_y$

TABLE 1. Symmetries of the component flows

Protocol	Sense of rotation	Flow	Symmetries
PA	Corotating	$F_B F_A$	S_y; $F_B S_x$
PA	Counter-rotating	$F_B F_A$	R^2; $F_B S_x$
PB	Corotating	$F_A^{\frac{1}{2}} F_B F_A^{\frac{1}{2}}$	S_x; $F_A^{\frac{1}{2}} F_B^{\frac{1}{2}} S_y$
PB	Counter-rotating	$F_A^{\frac{1}{2}} F_B F_A^{\frac{1}{2}}$	S_x; $F_A^{\frac{1}{2}} F_B^{\frac{1}{2}} R^2$

TABLE 2. Symmetries of time-periodic vortex mixing flows in square-wave form, assuming equal rotation speeds for F_A and F_B

corotating cylinder motion exhibits a symmetry along the y-axis and a *curved line of symmetry* along $F_B^{\frac{1}{2}}$ {x-axis}, i.e. the x-axis advected by flow B through half of its displacement. As we will see in the next section, this curved line of symmetry, although not visually apparent in the Poincaré sections, helps determine periodic points of the flow. A derivation of these symmetry relations is presented in the Appendix B.

A final note concerns the relation between geometric symmetries and the flow symmetries. The VMF geometry has three symmetries, reflections across the x- and y-axis and 180° rotations. The protocols of composed flows in table 2 have one flow symmetry that coincides with a geometric symmetry and one that does not because the sense of rotation in general breaks the geometric symmetries. The fact that a flow symmetry coincides with a geometric symmetry is a result of the overall phases of PA and PB being respectively 0 and $\frac{1}{4}$. Other phases turn both flow symmetries into curves that do not coincide with any geometric symmetries. The lesson here is that if the phase is chosen poorly, then flow symmetries are hidden, and from a practical point of view they cannot be exploited to reduce computational workloads, as is done for many of the tools described in §4.

4. Dynamical tools for use in mixing studies

In this section we describe several methods to calculate the dynamical characteristics of the chaotic flows under investigation. The presentation and evaluation is from the viewpoint of their direct bearing on the needs of mixing studies and, particularly, on possible limitations when extended to complex flows. The tools are arranged roughly according to computational effort.

4.1. *Poincaré sections*

Poincaré sections provide an asymptotic picture of the global behaviour of a flow. Poincaré maps are constructed from integration of a few selected initial points for hundreds if not thousands of periods, marking the location of the points at the end of each period. Since only a few points are involved, the calculations are swift even with numerically computed velocity fields. After many periods the marks reveal the long-time structure of the flow: regular regions or islands are shown as nested solid or broken lines; chaotic or well-mixed regions are shown as jumbles of points (although

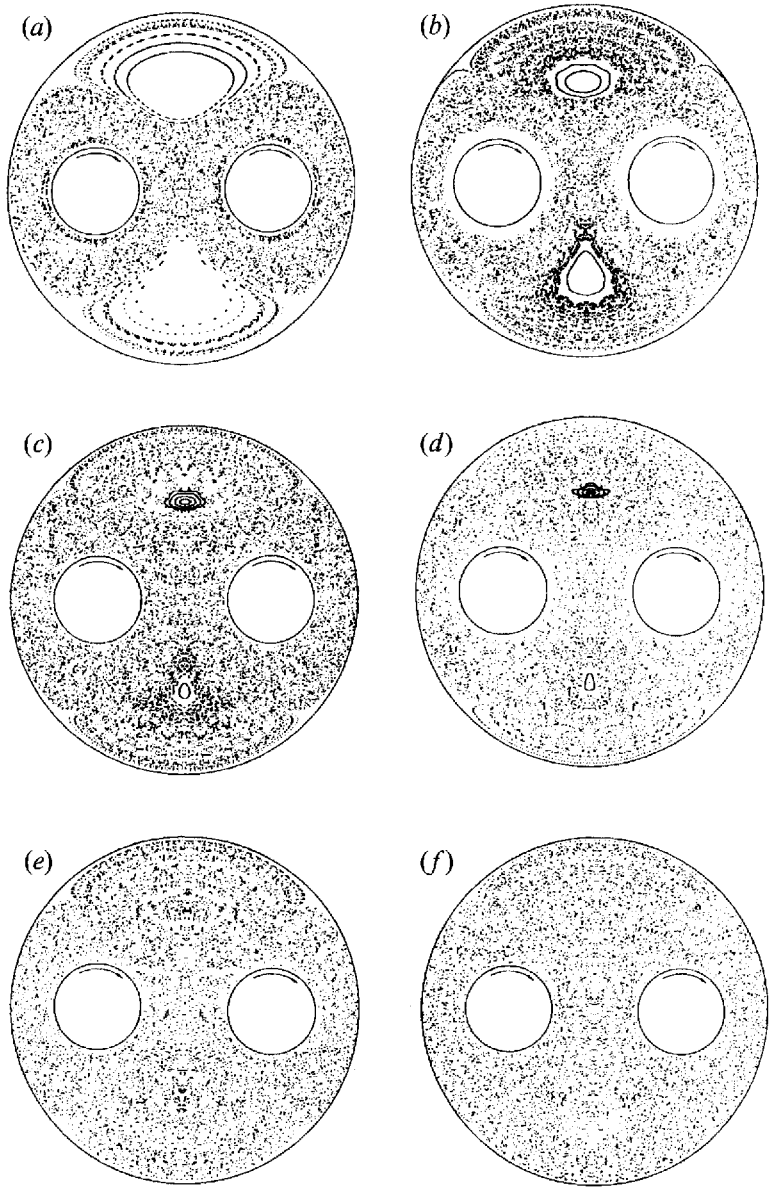

FIGURE 13. Poincaré sections of the vortex mixing flow using corotating cylinder motion with protocol A; $e = 0.67$, $R_o/R_i = 4.0$: (a) $\theta = 360°$, (b) $\theta = 540°$, (c) $\theta = 720°$, (d) $\theta = 900°$, (e) $\theta = 1080°$, (f) $\theta = 1440°$.

close examination may always reveal small-scale structures throughout the chaotic jumble).

Symmetries are clearly evident in the Poincaré sections of figures 13–15. Figure 13 uses PA with corotating cylinders; this protocol has $\boldsymbol{S}_y$ symmetry (table 2). Figure 14 uses PA with counter-rotating cylinders; this protocol has $\boldsymbol{R}^2$ symmetry. In fact, in computing the Poincaré sections the symmetry relations are exploited to reduce the computation workload, e.g. in figure 13 initial conditions are placed only on the left half-plane and advected; the mappings from initial conditions on the right half-plane are then obtained by reflection across the y-axis.

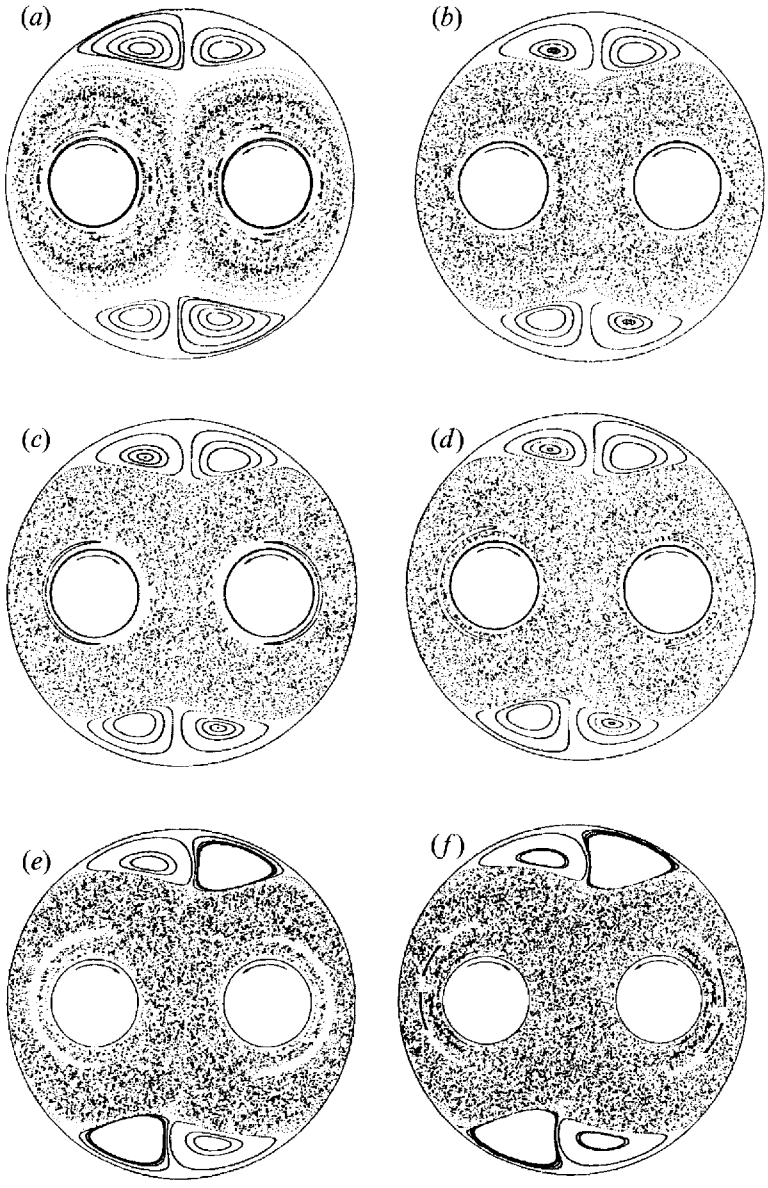

FIGURE 14. Poincaré sections of the vortex mixing flow using counter-rotating cylinder motion with protocol A; $e = 0.67$, $R_o/R_i = 4.0$: (*a*) $\theta = 360°$, (*b*) $\theta = 540°$, (*c*) $\theta = 720°$, (*d*) $\theta = 900°$, (*e*) $\theta = 1080°$, (*f*) $\theta = 1440°$.

Poincaré sections also provide a simple way to visually obtain a rough estimate of mixing characteristics and how they change with different protocols and parameter values. For instance, at lower values of θ the Poincaré sections in figure 13 show the appearance of two islands which do not move for any time t and are therefore defined as period-zero (P-0) islands. However, the size of these islands decreases with increasing θ and the islands cease to appear at all beyond a value of $\theta \approx 1182°$ as the elliptic points contained in the islands turn into hyperbolic points. The Poincaré sections of figure 14 show the opposite behaviour. The largest mixing zone develops at a value of θ as low as 540° and higher-period islands appear around the inner cylinders

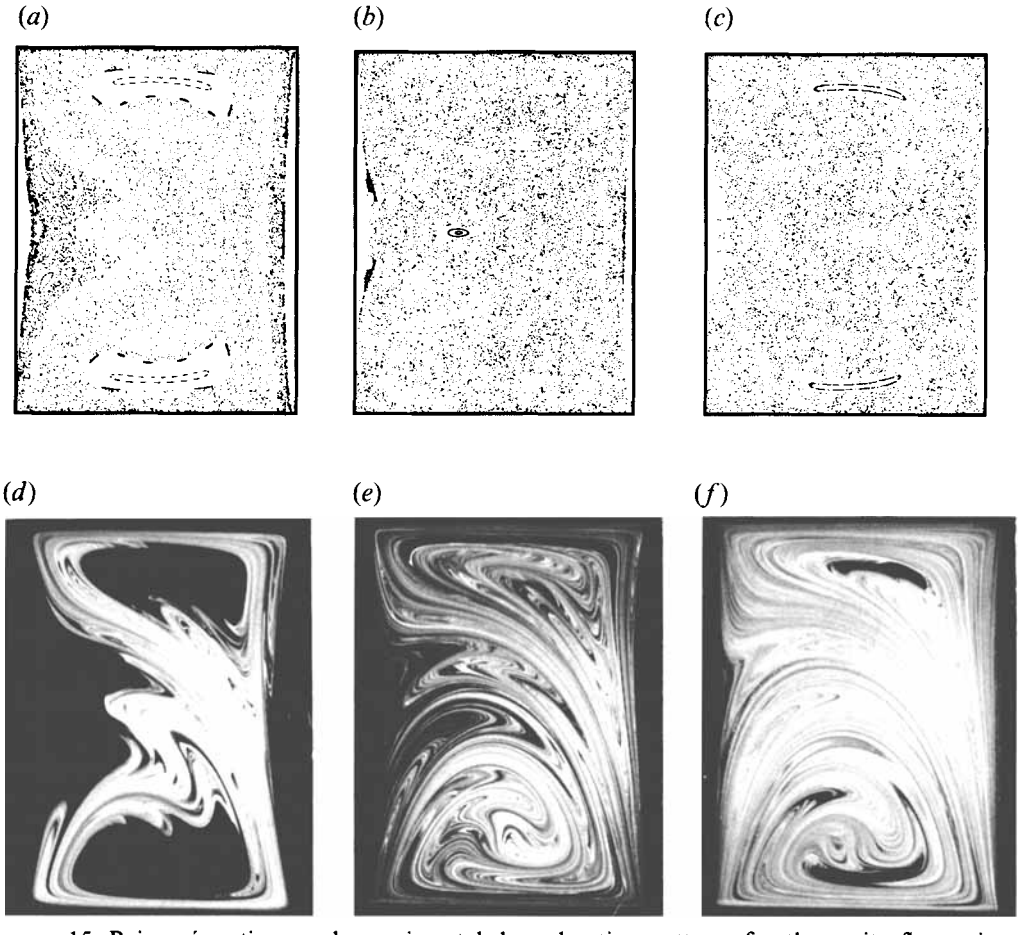

FIGURE 15. Poincaré sections and experimental dye advection patterns for the cavity flow using corotating top and bottom wall motion with protocol A; $A = 0.75$, $r = -1$, $H = 10.16$ cm, $W = 7.62$ cm. Poincaré sections: (*a*) $D = 4.62$, (*b*) $D = 6.93$, (*c*) $D = 9.24$. Experimental dye advection pattern after 6 periods: (*d*) $D = 4.62$, (*e*) $D = 6.93$, (*f*) $D = 9.24$.

with further increase in θ. At $\theta = 540°$, period-1 islands appear around each inner cylinder which bifurcate into higher-order chains at higher values of θ. The extent of the mixing region for the counter-rotating flows thus decreases at higher θ. Figure 15 shows Poincaré sections for cavity flows. The computations are done using a finite difference velocity field on a 49×81 grid with bicubic splines for interpolation. With PA this flow has an S_x symmetry which is exploited in figure 15(*a–c*). Two P-1 islands present at $D = 4.62$ disappear at $D = 6.93$ but appear again at $D = 9.24$. If D is increased further the P-1 islands disappear and reappear at even higher values of D; the sequence repeats itself. Experimental counterparts to figures 13, 14 and 15(*a–c*) are figures 15(*d–f*), 16 and 17; comparisons are discussed further in §4.2.

Poincaré sections are very easy to calculate especially in the presence of symmetries and give the asymptotic mixing structures of the flow, but one must be careful in trying to extrapolate from long-time results to anticipate the results of short-time dye advection experiments (such as those shown in figures 15*d–f*, 16, 17). When Poincaré sections show regular regions, dye advection experiments will typically show even larger islands in those regions as well. However, even if the Poincaré sections do not

exhibit any regular regions, we may not conclude that the flow mixes globally, because particle paths may appear regular for many periods, taking on the 'look' of chaotic motion only after hundreds or even thousands of periods of motion. It is important to stress that the Poincaré sections do not yield information about the rate of mixing.

4.2. *Dye advection experiments*

Dye advection is not exactly a dynamical tool; however, advection experiments or simulations of advection experiments are the only methods available for determination of short-time mixing patterns and rates. In this section we illustrate the difference between the development of mixing patterns after a few periods (not more than 10) and the asymptotic mixing expected from Poincaré sections. We also compare numerical dye advection calculations with experiments. Results show close agreement between BIEM computations and experiments.

Figures 15(*d–f*), 16 and 17 show experimental blob deformation patterns for the multicell cavity flow and the vortex mixing flow. Other eccentricities in the VMF are considered for the optimization test problem in §7. In figure 16, as expected from the Poincaré sections of figure 13, at lower values of θ the mixing is confined near the unperturbed homoclinic orbit of figure 9(*a*). As θ increases, the dye spreads out more towards the outer cylinder. A pair of P-0 islands are present up to $\theta \approx 1182°$. At $\theta = 1440°$, most of the flow region is covered by the dye in 8 periods of the flow except for some tiny unfilled regions scattered in the flow and a small neighbourhood of two parabolic points on the outer cylinder. However, the experiment cannot be carried out for long enough to check if those tiny unfilled regions would be covered by the dye; the striations thin out rapidly in most of the flow region, especially near the inner cylinders and molecular diffusion blurs the picture. The counter-rotating protocol in the VMF produces a poorer mixing flow than the corotating protocol. In figure 17 the area covered by the dye in this case reaches an asymptotic value at $\theta = 540°$ and at higher values of θ the area coverage decreases because of the appearance of higher-order islands near the inner cylinders. In figure 15(*d–f*) we show the dye advection pattern in the slender cavity flow. As the wall displacement per period increases, the area coverage in figure 15 increases dramatically from $D = 4.62$ to $D = 6.93$ and then decreases at $D = 9.24$ with the appearance of islands, once again in agreement with the Poincaré sections.

The results in figure 15 suggest the existence of *mixing windows* in the D-space of the cavity flows. Ling & Schmidt (1992) have considered this idea in an $A > 1$ cavity flow and assumed that a flow mixes well if P-1 islands do not exist as visualized in Poincaré sections. They showed specifically that, for a cavity flow with a fixed geometry and fixed wall velocity, mixing windows appears in bands in the displacement parameter, as evident in the Poincaré sections and dye advection experiment in figure 15. Consider these ideas in the context of our example. The islands formed in the vortex mixing flow by P-0 elliptic points disappear at higher values of θ. If there exists a critical value of θ beyond which there are no P-0 or P-1 islands in the flow and the mixing is global, the critical value of θ defines a *mixing window*. For the corotating vortex mixing flow with protocol A (figures 13 and 16), no higher-order (> 1) islands are found in the Poincaré sections and period-0 islands cease to appear at all beyond a critical value of $\theta \approx 1182°$ where the elliptic points of the islands turn into hyperbolic points. Any θ above 1182° produces global mixing in the vortex mixing flow with $R_o/R_i = 4$, $e = 0.67$, corotating cylinder motion, and square waveform. Let us now consider the limitations of this approach. One limitation of such an analysis is that it is based on Poincaré sections of the flow. Poincaré sections describe only the asymptotic mixing structure of the flow

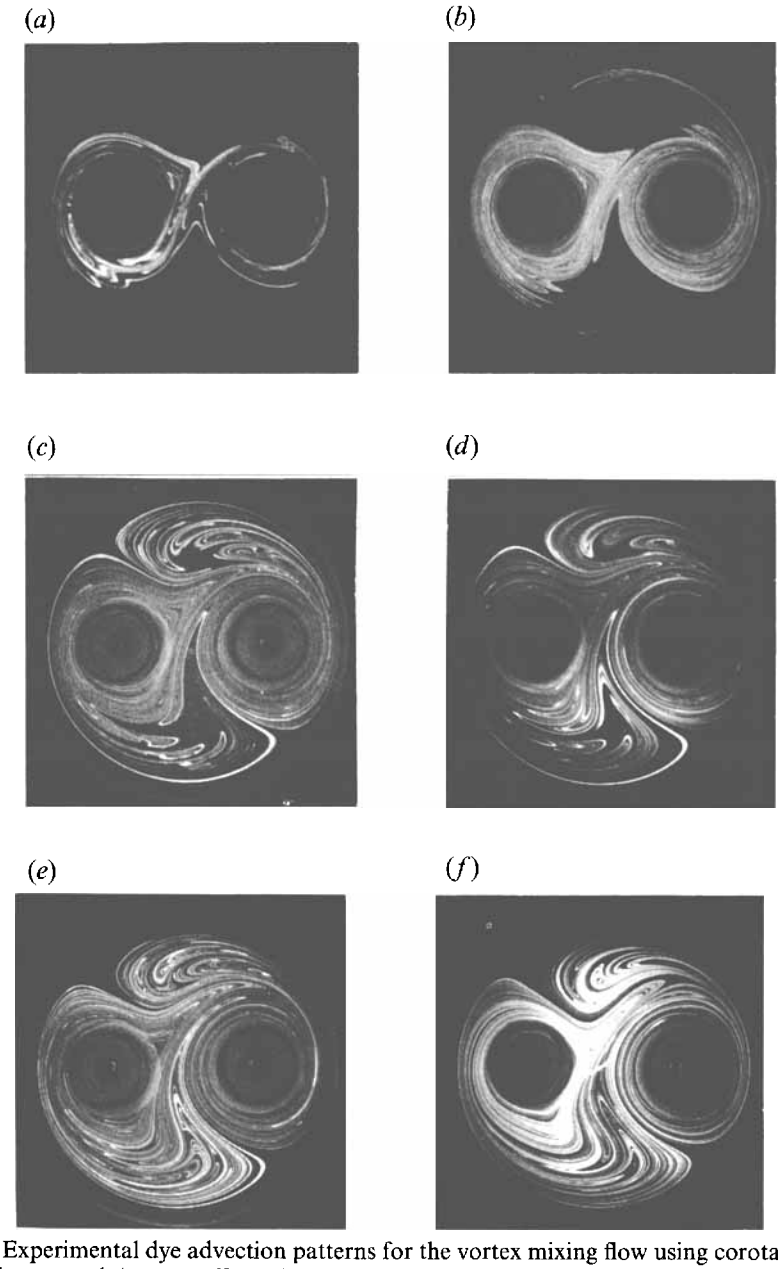

FIGURE 16. Experimental dye advection patterns for the vortex mixing flow using corotating cylinder motion with protocol A; $e = 0.67$, $R_o/R_i = 4.0$: (*a*) $\theta = 360°$ after 15 periods, (*b*) $\theta = 540°$ after 18 periods, (*c*) $\theta = 720°$ after 16 periods, (*d*) $\theta = 900°$ after 12 periods, (*e*) $\theta = 1080°$ after 10 periods, (*f*) $\theta = 1440°$ after 8 periods.

and do not yield any information about the rate at which this structure is achieved. The Poincaré section for a parameter set in the mixing window may not show any island, but the dye advection pattern in experiments which are carried out only for a low number of periods may contain several regions not filled with the dye and appearing as islands. Another limitation is that a flow might have higher-order elliptic periodic points leading to poor mixing, or the flow might still contain P-1 elliptic points but the islands be so small as to be inconsequential. Conversely, the flow might contain no P-1

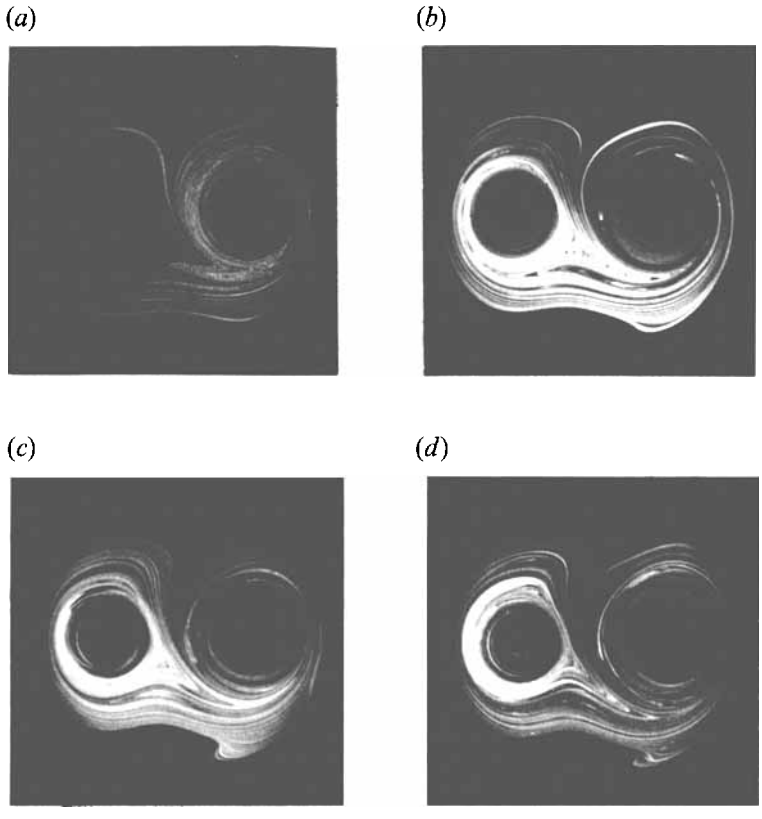

FIGURE 17. Experimental dye advection patterns for the vortex mixing flow using counter-rotating cylinder motion with protocol A; $e = 0.67$, $R_o/R_i = 4.0$: (*a*) $\theta = 360°$ after 24 periods, (*b*) $\theta = 540°$ after 16 periods, (*c*) $\theta = 720°$ after 15 periods, (*d*) $\theta = 1080°$ after 14 periods.

or P-3 elliptic points but the islands associated with P-3 or higher-order points might still be large. A good example of this behaviour appears in Leong & Ottino (1989*b*).

In figure 18 (Plate 1) a numerical simulation of blob deformation is compared with experiment. The initial blob is mimicked by a disk of 4000 points placed approximately at the location of the initial blob in the experiment. Each of these points is then advected using protocol A. To obtain the deformed blob after two periods in figure 18(*b*) the locations of 4000 points are plotted. At higher periods adjacent points separate and it becomes difficult to resolve the shape of the deformed blob. One remedy for this problem is to start with a larger number of points, but with exponential stretching pulling the points apart this method is very expensive. A computationally more attractive method is suggested by an experimental observation: in dye advection experiments the advection template developed in early periods from the action of the invariant unstable manifolds survives with time; the action of later periods is to add finer and finer levels of detail (Leong & Ottino 1989*a*, Swanson & Ottino 1990). In this method the locations of 4000 points are plotted starting from, say, the second period. For example, in figure 18 the locations of 4000 points after period-2, -3, -4, and -5 are plotted to get the deformed blob after 5 periods. In this way the computation time can be significantly reduced and sufficient resolution achieved by advecting a smaller number of points. While this method is strictly no longer a blob deformation simulation, it remains true to the goal of finding the blob deformation pattern. Figure 18 shows that all major folds in the experimental pictures can be numerically simulated.

Of course, one finds some differences in the fine scales; even with an analytical solution a perfect match of all striations and folds cannot be achieved because of truncation errors. Agreement at the finest scales can be improved by using a large number of boundary elements or by using curved boundary elements and/or interpolated boundary velocities and point source strengths. These numerical refinements will be addressed elsewhere (Jana *et al.* 1993).

4.3. *Periodic points, manifolds, and stretching*

Periodic points and their associated manifolds are the fundamental components of chaotic mixing patterns. It has been well demonstrated that elliptic points are at the centre of non-mixing regions called islands (although not all poorly mixing regions are islands), and that hyperbolic points are centres of stretching and folding in the flows. Less well demonstrated is that the mixing near parabolic points depends on whether the point, which occurs on surfaces in pairs, is a separation or reattachment point. The mixing is never good at separation points; the flow is always away from the surface and unstable manifolds cannot pile up. Unstable manifolds at reattachment points can pile up and the mixing can be vigorous (Camassa & Wiggins 1991). In this section we discuss methods to locate periodic points, particularly by exploiting symmetries, and show how manifold structures dictate the advection pattern. But beyond knowledge of the locations of periodic points, it is also important to discover the orbits of the periodic points and how that leads to interaction between the points and their manifolds. Finally we address the question of how indicative the local properties in the vicinity of the periodic points are of the global properties along the point's associated manifold.

Periodic points are at least as, if not more, important than critical points in determining mixing patterns. Figure 19 shows the orbits of period-1, period-2, and period-3 hyperbolic points of the VMF for $\theta = 1440°$ with PA. It is important to determine the motion of periodic points as they provide a template for the organized aspects of the flow. The most general way to locate period-n points in a flow is to integrate a candidate point for n-periods and see if it returns to its initial location. Things are much simpler if the flow has symmetries. For doubly symmetric systems periodic points can be located by exploiting both the symmetries. For instance, with a reflectional symmetry, all odd-order chains of periodic points, $n > 1$, must have one point on the symmetry axis, and all even-order chains of periodic points must have an equal number of points on either side of the symmetry axis. Period-1 points, on the other hand, stay either on the symmetry axis or appear in pairs about the symmetry axis. A general procedure for finding period-1 points is to find the *conjugate curves* of the flow symmetries. There are three steps to finding periodic points with this method. We refer to figure 20 and as an example find period-1 points on the conjugate curves in the VMF for $\theta = 1440°$, PA, and corotating cylinder motion. First, advect the line of geometric symmetry, which is the x-axis in this case (see figure 12). In figure 20(b) the x-axis is transformed into the *curved line of symmetry* after rotating the right inner cylinder through a rotation of 720° (i.e. $\boldsymbol{F}_B^{\frac{1}{2}}\{x\text{-axis}\}$, see table 2 and Appendix B). Next, in figure 20(c) this curve is reflected across the other symmetry axis (in this case the y-axis, see table 2) to make a second curve and together these curves constitute the conjugate curves of the flow. Finally, the intersection points of these curves locate the period-1 points. A check on the orbits of these points, which are found to be circular arcs about the inner cylinders, reveals that they indeed come back to their original location at the end of a period. These orbits are not shown in figure 19. A second set of period-1 points lies on the axis of symmetry as shown in figure 19. A linearization

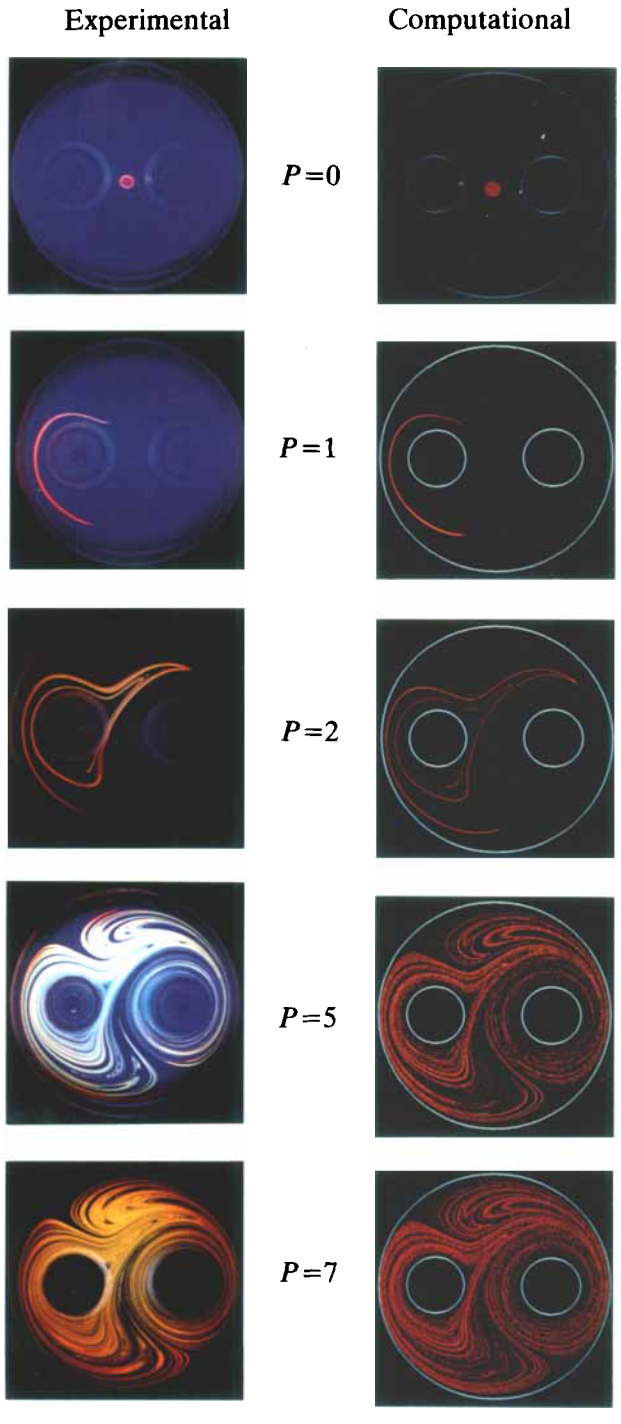

FIGURE 18. Comparison of numerical experiments on blob deformation (right) with experimental dye advection patterns (left) for the vortex mixing flow using corotating cylinder motion with protocol A; $e=0.67$, $R_o/R_i=4.0$, $\theta=1440°$; P is the elapsed number of periods.

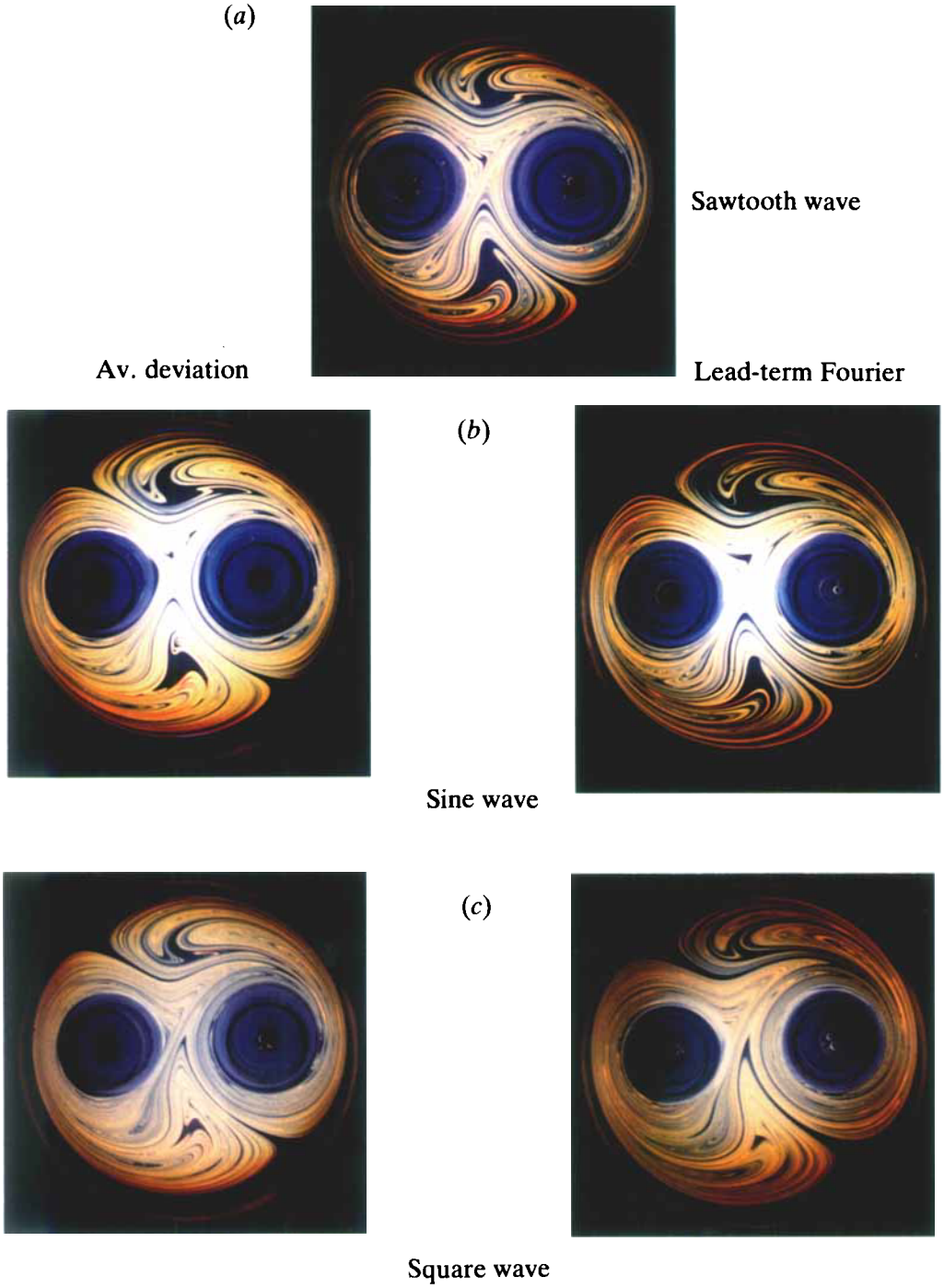

FIGURE 29. Experimental dye advection pattern for the vortex mixing flow. Corotating motion with protocol A; $e=0.67$, $R_o/R_i=4$, $\theta=1440°$ after 10 periods: (*a*) sawtooth wave with $\epsilon=1$, (*b*) sine wave, (*c*) square wave. In (*b*) and (*c*) the patterns on the left represent results with ϵ from average deviation and on the right with ϵ from the lead term of the Fourier series.

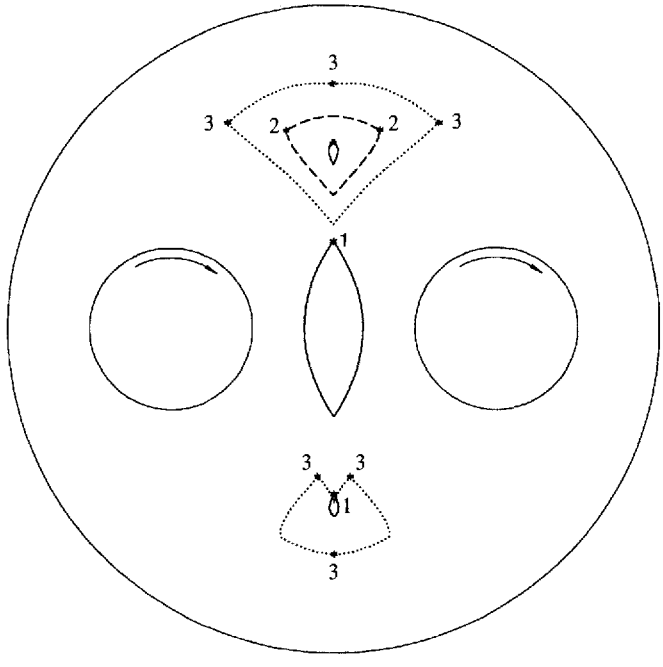

FIGURE 19. Orbits of the periodic point after three periods for the vortex mixing flows; $e = 0.67$, $R_o/R_i = 4$, $\theta = 1440°$, corotating cylinder motion. Solid lines are for P-1 points, dashed lines are for chains of P-2 points, and dotted lines are for chains of P-3 points. Some of the orbits of the points appear to overlap but the points never occupy the same orbit at the same time.

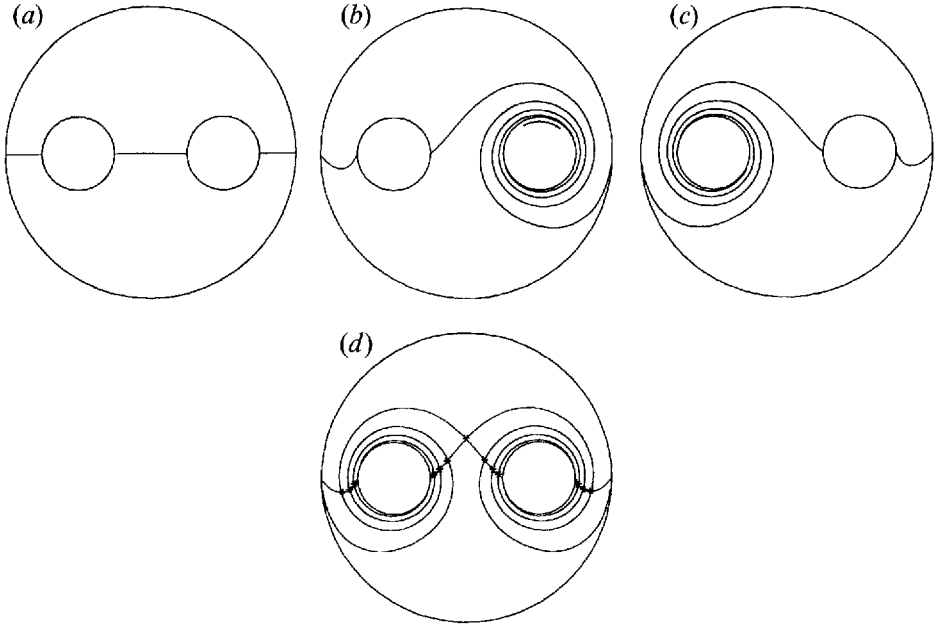

FIGURE 20. Conjugate curves and the location of P-1 points at the intersection of the conjugate curves for the vortex mixing flow; $R_o/R_i = 4$, $e = 0.67$, $\theta = 1440°$, corotating cylinder motion: (*a*) initial line on the *x*-axis, (*b*) the curved line of symmetry obtained by advecting the initial line by rotating the right inner cylinder through 720°, (*c*) mirror image of the curved line of symmetry on the *y*-axis, (*d*) conjugate curves. Periodic points are denoted by asterisks.

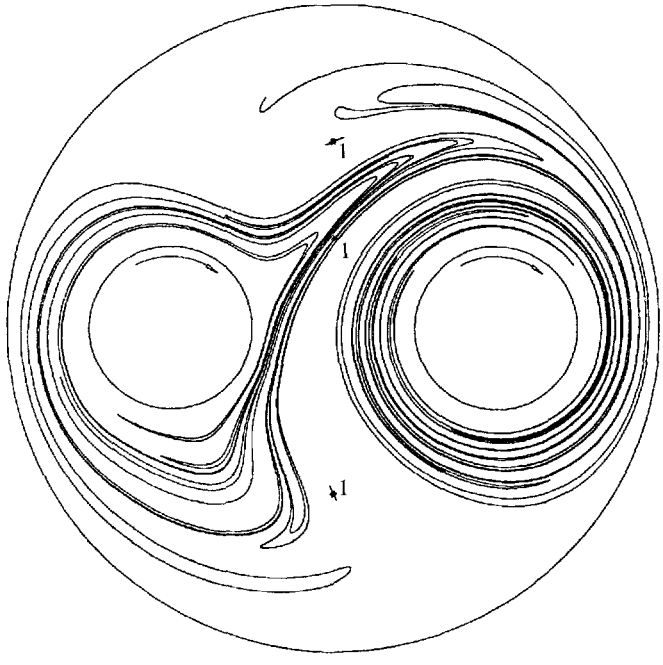

FIGURE 21. Unstable manifolds of P-1 points (denoted by *) up to 3 periods for the vortex mixing flow using protocol A for $\theta = 1440°$, $e = 0.67$, corotating cylinders, and $R_o/R_i = 4$.

of the flow around a periodic point determines the character of the point, hyperbolic or elliptic. The P-1 points found in figure 20 on the conjugate curves turned out to be all hyperbolic. This explains why fluid elements in the neighbourhood of the inner cylinders experience large stretching and why striations thin out rapidly in those regions.

To quantify stretching, define an infinitesimal material vector $\mathrm{d}\boldsymbol{X}_i$ initially located at a point $\boldsymbol{X}_i$ with an orientation $\boldsymbol{M}_i$ that stretches and deforms with the flow. Its length stretch λ is given by

$$\lambda = |\boldsymbol{DF}(\boldsymbol{X}_i)\cdot\boldsymbol{M}_i|, \tag{15}$$

where $\boldsymbol{DF}(\boldsymbol{X}_i)$ is the Jacobian matrix of the mapping $\boldsymbol{F}$ evaluated at $\boldsymbol{X}_i$. As the vector $\mathrm{d}\boldsymbol{X}_i$ deforms its orientation changes and after one period of the flow is given by

$$\boldsymbol{M}_{i+1} = \boldsymbol{DF}(\boldsymbol{X}_i)\cdot\boldsymbol{M}_i/\lambda, \tag{16}$$

where $\boldsymbol{X}_{i+1} = \boldsymbol{F}(\boldsymbol{X}_i)$ is the new location of the point. The stretching field of the flow $\lambda(\boldsymbol{x}, t)$ is obtained by averaging several vectors over all orientations. The eigenvalues of the hyperbolic periodic points determine the local rate of stretching and the eigenvectors determine the local directions of stretching and contraction. In the case of higher-order hyperbolic periodic points the eigenvalues of all the points in the chain are the same. Thus, the local rate of stretching at a periodic point is a property of the chain.

The manifold structures of hyperbolic periodic points are responsible for the advection pattern of material elements and are central to the understanding of the dynamics of fluid mixing. In what follows we use the algorithm described by Hobson (1993) to calculate the stable and unstable manifolds.

In almost all cases only a few or one of the lower-order hyperbolic periodic points contribute to the creation of the mixing template; the other hyperbolic points add the

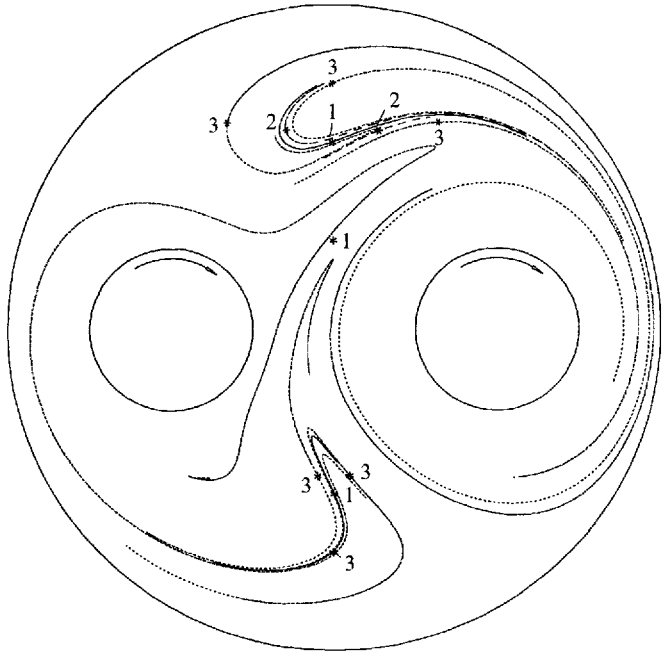

FIGURE 22. Unstable manifolds of P-1, P-2, and P-3 points up to 6 periods for the vortex mixing flow using protocol A for $\theta = 1440°$, $e = 0.67$, corotating cylinders, and $R_o/R_i = 4$. Solid lines are for P-1 points, dashed lines for P-2, and dotted lines for P-3 points. For clarity the manifold of the central P-1 point of figure 21 is not shown.

fine structure. Therefore, the extent of the main unstable manifold determines if the flow globally mixes. Because of the highly ramified nature of the tangled manifold, the length is infinite, but this infinite length is packed into a subdomain of the entire flow domain. Good mixing flows have their mixing template extended throughout the flow domain. It has been common wisdom in mixing studies that only the lower-order periodic points govern the dynamics of mixing and transport, but in complex flows the question is to decide which of the periodic points' manifolds are most important. While it is the usual case for the manifolds of some period-1 point to be the most important to the mixing character of the flow, it is not true that all period-1 points are more important than all higher-order periodic points. Consider the VMF as an example. Figure 21 shows the calculated unstable manifolds of the period-1 hyperbolic points of figure 19 after three periods. The central period-1 point controls the template of mixing for this case because its manifold develops quickly. This is a result of the relatively larger stretching along this manifold. In figure 22 the manifold structure of the central period-1 point from figure 21 is not drawn so that the effects of the other two period-1 points, two period-2 points, and all period-3 points of figure 19 may be more easily seen and compared. The extent of the period-3 manifolds is much larger than the two period-1 points and all period-2 points. Figure 23 shows another example where the stretching along the unstable manifold of a P-2 point calculated up to 6 periods is almost a factor of two larger than that along the largest stretching of the P-1 point. This exemplifies a case where the lowest-order periodic points do not entirely govern the dynamics.

It is also found that the stretching along manifolds bears little correspondence to the eigenvalues of the periodic points even after one period of the flow. Figure 24 shows the unstable manifolds of three P-3 points of the same chain along with their orbit for

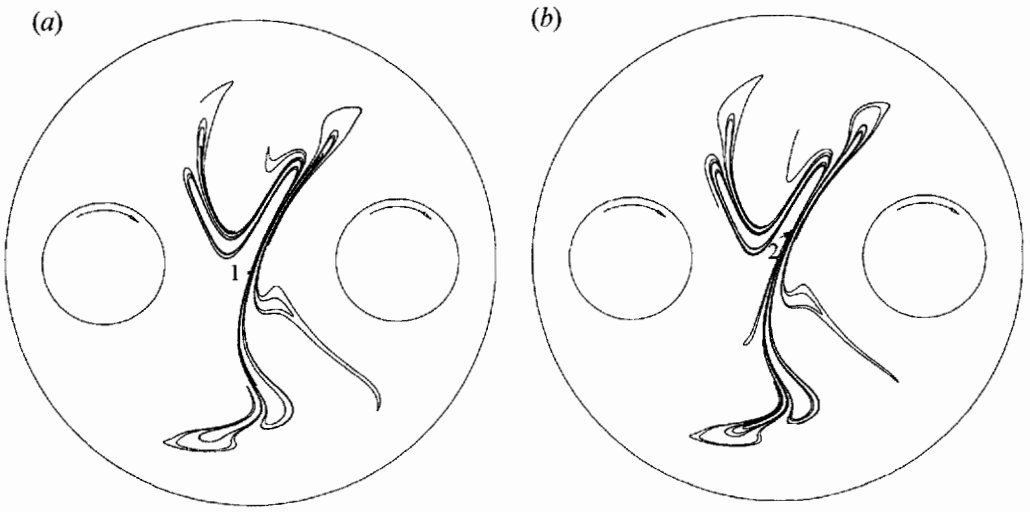

FIGURE 23. Comparison of unstable manifolds of (*a*) a P-1 point and (*b*) a P-2 point after 6 periods in the vortex mixing flow using protocol A for $\theta = 1440°$, $e = 0.80$, corotating cylinders, and $R_o/R_i = 4$. Stretching along the manifold of the P-2 point is almost a factor of two more than the P-1 point.

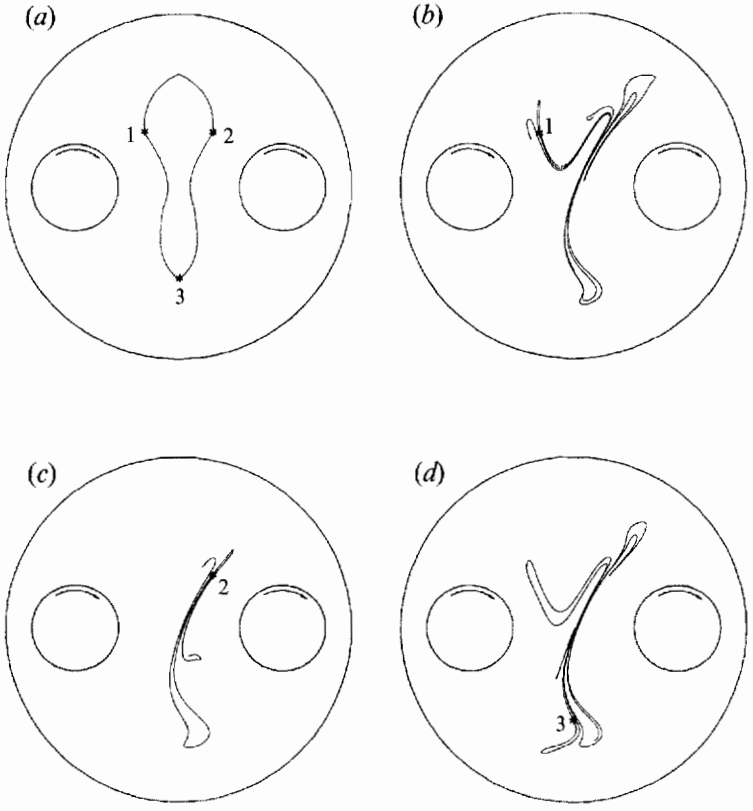

FIGURE 24. Unstable manifolds of a P-3 chain with the three P-3 points labelled 1, 2, and 3 after 6 periods in the vortex mixing flow using protocol A, $\theta = 1440°$, $e = 0.80$, corotating cylinders, and $R_o/R_i = 4$; (*a*) orbit of P-3 point, (*b–d*) manifolds of points 1–3 respectively. The cumulative stretching along manifolds is presented in table 3.

Period	Point 1	Point 2	Point 3
3	300	630	640
6	18000	9500	28500

TABLE 3. Comparison of stretching along manifolds of three P-3 points of the same chain shown in figure 24; $\theta = 1440°$, $e = 0.8$, PA, $R_o/R_i = 4$, corotating cylinder motion

the vortex mixing flow. Although these periodic points have equal eigenvalues, the stretching values along the unstable manifolds are different as shown in table 3. Also, the trend found after 3 periods does not hold after 6 periods as the portions of the manifolds traverse different environments once they emerge from the vicinity of the periodic points. This shows that the stretching characteristics of all periodic points of a higher-order chain cannot be obtained by studying only one periodic point of the chain. These issues must be taken into account when making comparisons regarding the mixing characteristics of flows. It is wise to compare the stretching values along the unstable manifolds rather than comparing just the eigenvalues of the periodic points. The unstable manifolds must be calculated for a reasonable number of periods to allow for interaction with other periodic points.

Although the manifold structures and stretching along manifolds produce a clear picture about the role of various periodic points in dictating the dynamics of mixing, information about the global mixing characteristics is difficult to extract from them. The global mixing pattern is a result of the cumulative action of the manifolds of numerous hyperbolic periodic points of various orders and it is computationally taxing to study each of them separately and include them in the analysis. An alternative tool specifically suited to this purpose is the calculation of stretching values for a large number of points uniformly distributed in the flow and to study their distribution. The distribution of stretching values within a flow shows remarkable agreement with dye advection structures. Moreover, the probability density function of stretching provides quantitative information regarding the quality of mixing in the flow. Calculation of stretching of material elements in chaotic flows is computationally expensive and difficult if the velocity field is numerically evaluated. In spite of such difficulties, stretching plots and distributions of stretching values (DSV) have become useful tools in quantifying mixing in chaotic flows. Muzzio, Swanson & Ottino (1991) showed that in chaotic flows the DSV follows a log-normal distribution and the shape of rescaled distribution curves are time invariant after a few periods of the flow. In §7 we use the DSV to compare the mixing structures produced at various eccentricities in the VMF.

4.4. *The Melnikov method*

The Melnikov method provides one of the few analytical tools for the analysis of chaotic flows. In steady flows stable and unstable manifolds coincide leading to the regular closed orbits that are the hallmark of steady flows. When perturbed, the stable and unstable manifolds separate but still intersect at a set of homoclinic or heteroclinic points. The manifolds between intersections loop away from the unperturbed orbit to form lobes. These lobes play a central role in the mixing and transport of dynamical systems.

A form of the equations of motion suitable for use with Melnikov's method is

$$\frac{\mathrm{d}\boldsymbol{x}}{\mathrm{d}t} = \boldsymbol{f}(\boldsymbol{x}) + \epsilon \boldsymbol{g}(\boldsymbol{x}, t), \quad t \in (0, T), \tag{17}$$

where $f_1 = \partial\psi_0/\partial x_2, f_2 = -\partial\psi_0/\partial x_1$, $g_1 = \partial\psi_1/\partial x_2$, $g_2 = -\partial\psi_1/\partial x_1$, ϵ is a perturbation, and $\psi(x_1, x_2, t) = \psi_0(x_1, x_2) + \epsilon\psi_1(x_1, x_2, t)$ is the streamfunction of the perturbed flow.

The Melnikov method (Guckenheimer & Holmes 1983; Wiggins 1988) checks the transverse intersection between the stable and unstable manifolds of a hyperbolic point to find the distance between the perturbed manifold and its previous location on the unperturbed homoclinic orbit. The distance $d(t_0)$ is given in terms of the Melnikov function $M(t_0)$ as

$$d(t_0) = \frac{\epsilon M(t_0)}{|\boldsymbol{f}[\boldsymbol{q}^{(0)}(t)]|} + O(\epsilon^2), \tag{18a}$$

$$M(t_0) = \int_{-\infty}^{+\infty} \{\boldsymbol{f}[\boldsymbol{q}^{(0)}(t-t_0)] \wedge \boldsymbol{g}[\boldsymbol{q}^{(0)}(t-t_0), t]\}\,\mathrm{d}t, \tag{18b}$$

where $\boldsymbol{f}$ and $\boldsymbol{g}$ are derived from the flow through (17) and ' $\wedge$ ' is the wedge product $\boldsymbol{f} \wedge \boldsymbol{g} = f_1 g_2 - f_2 g_1$; $\boldsymbol{q}^{(0)}$ is the unperturbed homoclinic orbit, ϵ is the perturbation parameter, and t_0 is the time when the distance $d(t_0)$ is being calculated. The Melnikov method can be used to detect the presence of chaos: one intersection implies infinitely many and infinitely many intersections implies a homoclinic tangle and hence chaos. It should nevertheless be remarked that in most mixing problems the existence of chaos is usually not at issue – it is rather easy to predict which flows will give rise to chaos and which ones will not. Rather, the utility of Melnikov's method is to characterize and quantify the effects of chaos on mixing and transport.

Consider now the application of the method, especially in the context of numerically calculated velocity fields. The streamfunction of the perturbed flow is a linear combination of the streamfunction of the flows produced by each moving element, for example, the left and right inner cylinders in the vortex mixing flow:

$$\psi(x_1, x_2, t) = U(1 + \epsilon f(t))\,\psi_A(x_1, x_2) + U(1 - \epsilon f(t))\,\psi_B(x_1, x_2). \tag{19}$$

The streamfunctions $\psi_A(x_1, x_2)$ and $\psi_B(x_1, x_2)$ correspond to the flows produced by moving the elements A and B respectively at unit velocity. After simplification, (19) can be written as

$$\psi(x_1, x_2, t) = \psi_0(x_1, x_2) + \epsilon\psi_1(x_1, x_2, t), \tag{20}$$

where

$$\psi_0(x_1, x_2) = U(\psi_A(x_1, x_2) + \psi_B(x_1, x_2)), \tag{21a}$$

$$\psi_1(x_1, x_2, t) = U(\psi_A(x_1, x_2) - \psi_B(x_1, x_2))f(t). \tag{21b}$$

The Melnikov method gives the number of transverse intersections between the stable and unstable manifolds per period, i.e. the zeros of $M(t_0)$ as well as the lobe area, valuable information which could otherwise be gathered only by examination of numerous specific computations. The *lobe area* μ is defined as the area formed by the segments of the stable and unstable manifolds between two consecutive intersections at τ_1 and τ_2 and is given as

$$\mu = \epsilon \int_{\tau_1}^{\tau_2} M(\tau)\,\mathrm{d}\tau + O(\epsilon^2) \tag{22}$$

(Rom-Kedar, Leonard & Wiggins 1990; Wiggins 1992). Lobe area is a measure of the degree of chaos – a zero lobe area means no chaotic motion. Using (17), (18), and (20), $M(t_0)$ can be written as

$$M(t_0) = 2\int_{-\infty}^{+\infty} (u_{1B}\,u_{2A} - u_{1A}\,u_{2B}) f(t + t_0)\,\mathrm{d}t, \tag{23}$$

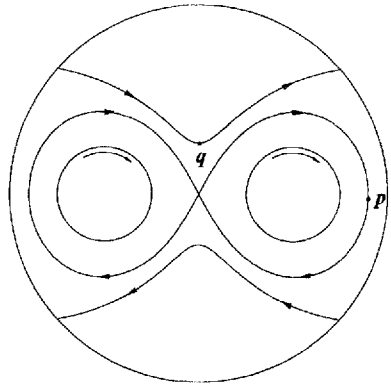

FIGURE 25. Unperturbed homoclinic and heteroclinic orbits for the vortex mixing flow; $R_o/R_i = 4$, $e = 0.67$, and $r = 1$. The points $\boldsymbol{p}$ and $\boldsymbol{q}$ are the starting points for the evaluation of the Melnikov integral.

where u_{iK}, $i = 1, 2$, is the ith component of the velocity at a point on the unperturbed homoclinic orbit produced by the moving element $K(K = A, B)$. It can be easily proved with the aid of (23) that streamline crossing is a necessary and sufficient condition for chaos in bounded two-dimensional fluid flow (i.e. $\boldsymbol{u}_A(\boldsymbol{P}, t_1) \neq k\boldsymbol{u}_B(\boldsymbol{P}, t_2)$, for some point $\boldsymbol{P}$).

In order for the Melnikov method to be used, the homoclinic orbit must be known accurately. A closed-form analytical expression for $M(t_0)$ can be obtained if $u_{iA,B}$ are given analytically in terms of t. However, for complex flows the homoclinic orbit is almost never known analytically and (23) must be evaluated by integrating simultaneously with following a point on the homoclinic orbit. In the vortex mixing flow to obtain the homoclinic and heteroclinic orbits accurately, we use respectively 200 and 50 boundary segments distributed symmetrically on the outer cylinder and each of the inner cylinders. Figure 25 shows the double homoclinic orbits of the hyperbolic point and the heteroclinic orbits of the parabolic points. To test that the homoclinic orbit is accurately obtained, we advect a point starting at the hyperbolic point for one traversal of the homoclinic loop. If the point returns tolerably close (within 10^{-10} say) to its starting location, then the velocity is accurate enough. If the velocity field is not accurate enough, the point would never return to the close proximity of the hyperbolic point and an acceptable homoclinic loop cannot be obtained. For example such a difficulty may arise when the velocity is evaluated by interpolation from the nodal values in finite difference or finite element methods.

To accommodate various waveforms in the analysis, $f(t+t_0)$ in (23) is expanded in a Fourier series:

$$f(t+t_0) = \sum_{i=1}^{\infty} C_i \cos\left(\frac{2\pi i(t+t_0)}{T}\right), \tag{24}$$

where C_i is the ith Fourier coefficient. The Melnikov integral can then be expressed as

$$M(t_0) = \sum_{i=1}^{\infty} C_i \left(M_i \cos\left(\frac{2\pi i t_0}{T}\right) - N_i \sin\left(\frac{2\pi i t_0}{T}\right)\right), \tag{25}$$

where

$$M_i = 2\int_{-\infty}^{+\infty} (u_{1B}u_{2A} - u_{1A}u_{2B}) \cos\frac{2\pi i t}{T}\,\mathrm{d}t \tag{26}$$

i	N_i
1	1.761×10^{-2}
3	3.733×10^{-4}
5	1.768×10^{-5}
7	9.850×10^{-6}
9	7.700×10^{-6}
11	6.310×10^{-6}
13	5.270×10^{-6}
15	4.540×10^{-6}
17	4.060×10^{-6}
19	3.650×10^{-6}

TABLE 4. Values of N_i along the right homoclinic loop of figure 25; $R_o/R_i = 4$, $e = 0.67$, $\theta = 540°$, sine waveform and corotating cylinder motion

and
$$N_i = 2\int_{-\infty}^{+\infty} (u_{1B}\, u_{2A} - u_{1A}\, u_{2B}) \sin\frac{2\pi i t}{T}\,\mathrm{d}t. \tag{27}$$

The integrals M_i can be shown to vanish by starting the integration from the symmetric points $\boldsymbol{p}$ and $\boldsymbol{q}$ on the unperturbed homo- and heteroclinic orbits, as shown in figure 25. The integrals N_i always converge as a point on the homoclinic loop approaches the hyperbolic point. Similar arguments hold for the heteroclinic connections of figure 25. The zeros of $M(t_0)$ are given by the zeros of $\sin(2\pi i t_0/T)$ which are at $t_0 = T/2$ and T. So the stable and unstable manifolds intersect each other twice in a period, forming two lobes. Evaluating (22) the lobe area is

$$\mu = \frac{T}{\pi}\sum_{i=1}^{\infty}\frac{C_i N_i}{i}. \tag{28}$$

In §5 we use sine waves, square waves, and sawtooth waves for $f(t)$. Note that $C_i = 0$ for i even for the square and sawtooth waves and that (28) has only one term for a sine wave. Therefore we need only calculate the integrals for i odd. The first ten non-zero values of N_i are tabulated in table 4 for the flow of figure 25. N_1 is almost two orders of magnitude larger than the subsequent terms. In §§5 and 7 we use lobe area to compare the effect of different waveforms and eccentricities on mixing.

A limitation of the standard version of the Melnikov method is its formal restriction to small perturbations. In this version of the Melnikov method a perturbation is regarded as valid and 'small' as long as $d(t_0)$ in (18) is single valued. If the manifold structures become convoluted above some value of ϵ, the distance between the manifolds and the unperturbed homoclinic orbit becomes multiple valued, as shown in figure 26 for the VMF. When this happens the Melnikov method ceases to apply. It should also be noted that Kaper & Wiggins (1993) have recently developed extensions to the standard Melnikov method for use with $O(1)$ perturbations. The value of ϵ beyond which the standard Melnikov method fails depends on the specific problem at hand. In the VMF using a sine waveform for the boundary motion, the Melnikov method is found to be valid for $\epsilon \leqslant 0.1$. Another drawback of the method is that the unperturbed system must possess a heteroclinic or homoclinic orbit. All the flows studied in this work exhibit at least one heteroclinic orbit or a pair of homoclinic orbits and the Melnikov method applies to all of them. However, for the $A = 1.67$ cavity flow and corotating wall motion – the most studied case to date and by no means an atypical situation – the unperturbed flow does not have homoclinic or heteroclinic

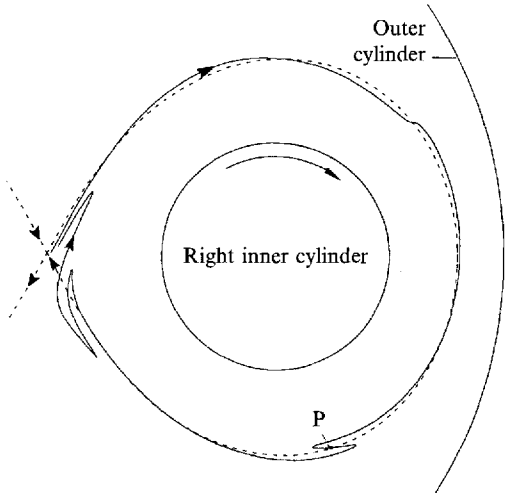

FIGURE 26. The Melnikov method breaks down for larger perturbations when the distance of the unstable manifold from the unperturbed homoclinic orbit becomes multivalued. The perturbed unstable manifold (solid line) corresponding to the right unperturbed homoclinic loop (dashed line) of figure 25 is shown. The sine waveform, $\epsilon = 0.25$, $\theta = 540°$, $e = 0.67$, $R_o/R_i = 4.0$, and corotating cylinder motion is used.

connections (Chien *et al.* 1986; Leong & Ottino 1989*a*). This drawback, however, can be circumvented by using a special form of the Melnikov method called the subharmonic Melnikov method (Guckenheimer & Holmes 1983) which has been used on the corotating journal bearing flow by Swanson (1991).

5. Effect of waveforms

How sensitive are mixing structures to the details of the forcing? We have seen how the total displacement, being proportional to the energy flux through a system, markedly changes mixing structures, destroying or creating islands, moving and changing the size and number of large folds, for instance. But given a fixed displacement, what are the effects of changing the forcing's overall phase and waveform, or the relative phase of the boundary motions, or the period of the motions? We have already seen in §3.3 how changes in the overall phase hide or expose symmetries. It may seem surprising that a time period could have any effect in a Stokes flow; the question requires a more detailed answer and is addressed in §6. To our knowledge no one has investigated the effects of systematic changes to the relative phase of boundary motions; motions are always fixed at π out of phase. In this section we focus on the effects of different forcing waveforms on mixing structures. To date several waveforms are commonly used to generate out-of-phase boundary motions: sine waves, square waves, and sawtooth waves. The main result of this section is that neither short-time advection patterns, nor asymptotic Poincaré sections depend on the specifics of the boundary motion.

The simplest qualitative argument suggesting this 'universality' of waveform is to consider the symmetrized version of (11) for the form of the boundary motions

$$u_A = U(1+\epsilon f(t)), \quad u_B = U(1-\epsilon f(t)), \tag{29a, b}$$

with the waveform $f(t)$ taken to be an undulatory function. If we expand f in a Fourier

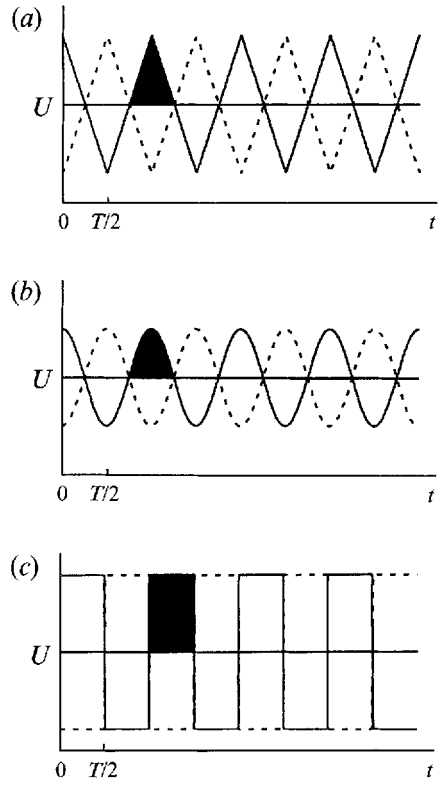

FIGURE 27. Common waveforms used to drive chaotic advection patterns: (*a*) sawtooth wave, (*b*) sine wave and (*c*) square wave.

series and if that series decays rapidly enough that the shape of f is substantially captured by the lead term of the series, then we should be able to truncate the series at the first term and by adjusting the lead coefficient, which becomes a rescaled ϵ, tune all waveforms to give the same forcing effects. Swanson (1991) presented a computational study on the effects of different waveforms on chaotic advection in an eccentric cylinder flow. He showed that qualitatively similar Poincaré sections can be found for all waveforms by the adjustment of the perturbation parameter. Three methods were used in that study to calculate the perturbation parameter: (i) equal average deviation from the mean velocity, (ii) identical lead term in the Fourier series, and (iii) equal distance between the stable and unstable manifolds calculated using the Melnikov method. In this study we use the same methodology to calculate the perturbation parameters and compare the performance of the sine wave, square wave, and sawtooth wave in terms of Poincaré section and experimental dye advection for the VMF. Equations (30)–(32) show formulae for the three waveforms and figure 27 shows representative sketches of each. In (30)–(32) since U is always positive we are showing results for corotating protocols; similar results hold for counter-rotating protocols.

Sawtooth wave:

$$u_1 = \begin{cases} U[1-\epsilon(4t/T-1)]; & 0 \leqslant t \leqslant T/2, \\ U[1+\epsilon(4t/T-3)]; & T/2 \leqslant t \leqslant T, \end{cases} \quad u_2 = \begin{cases} U[1+\epsilon(4t/T-1)]; & 0 \leqslant t \leqslant T/2, \\ U[1-\epsilon(4t/T-3)]; & T/2 \leqslant t \leqslant T. \end{cases} \tag{30}$$

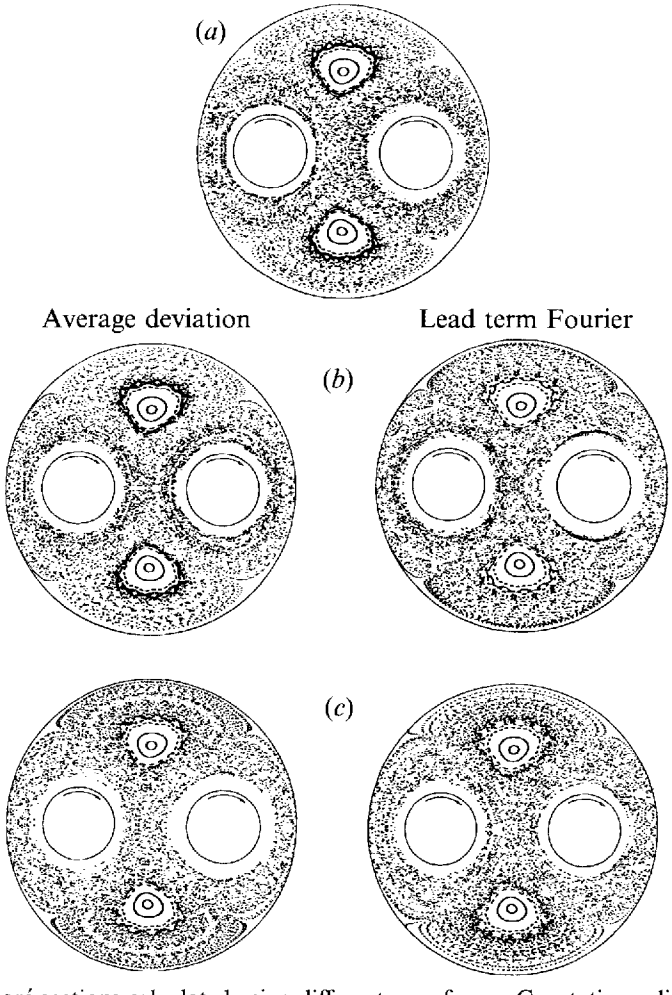

FIGURE 28. Poincaré sections calculated using different waveforms. Corotating cylinder motion with protocol A, $e = 0.67$, $R_o/R_i = 4$, and $\theta = 540°$: (*a*) sawtooth wave with $\epsilon = 1$, (*b*) sine wave, (*c*) square wave. In (*b*) and (*c*) the section on the left represents results with ϵ determined from average deviation and on the right with ϵ determined from the lead term of the Fourier series.

Method	Sawtooth wave (reference value)	Sine wave	Square wave
Average deviation from mean velocity	1.0	$\pi/4$	0.5
Lead term in Fourier series	1.0	$8/\pi^2$	$2/\pi$
Lobe area from the Melnikov method	1.0	$8/\pi^2$	$2/\pi$

TABLE 5. Values of perturbation parameter ϵ from different methods

Sine wave:

$$u_1 = U[1+\epsilon\cos(2\pi t/T)], \quad u_2 = U[1-\epsilon\cos(2\pi t/T)]. \tag{31}$$

Square wave:

$$u_1 = \begin{cases} U[1+\epsilon]; & 0 \leqslant t \leqslant T/2, \\ U[1-\epsilon]; & T/2 < t \leqslant T, \end{cases} \quad u_2 = \begin{cases} U[1-\epsilon]; & 0 \leqslant t \leqslant T/2, \\ U[1+\epsilon]; & T/2 < t \leqslant T. \end{cases} \tag{32}$$

If both inner cylinders in the VMF rotate at the mean speed U, the fluid particles follow regular orbits and there is no chaotic motion. The degree of chaotic motion is determined by the extent to which each cylinder rotates away from the mean speed U and is out-of-phase with the other. We use three ways to establish a match in the effect of waveforms. In the first method the shaded area under the curve in figure 27, which is a measure of the deviation from the mean velocity U, is made equal for each waveform by adjusting the respective ϵ values. The second method is based on the truncated Fourier series of the functions $f(t)$. The general form of the lead term in the Fourier series is $f(t) \approx C\cos(2\pi t/T)$, where C is a function of ϵ and depends on the specific waveform. The waveforms are then matched by adjusting the values of ϵ such that all of them have the same value of C. The third method uses the Melnikov method to calculate lobe areas (§4.4). The area of a lobe is a measure of the degree of chaos – a zero lobe area means no chaos – and the ϵ for different waveforms are adjusted to produce equal lobe areas. Although this last method is best for equalizing dynamical effects as it is based on the dynamics of the hyperbolic periodic points of the flow, it is difficult to implement except at low perturbation from integrability. In table 5 we present the values of ϵ calculated from the three methods. We set $\epsilon = 1$ for the sawtooth wave and calculate the relative ϵ values for the other waveforms.

Figure 28 shows a comparison of Poincaré sections. Identical initial conditions were used in all the computations. (Since the Melnikov method uses a Fourier series to calculate lobe area [28], it happens that the adjustments to ϵ from the Melnikov and lead-term Fourier series methods are identical. Therefore, we omit showing separate results in figures 28 and 29.) A lower value of θ is chosen in this case to show the presence of both chaotic and regular regions for a better comparison. Except for minor variations in the chaotic region the agreement is excellent. Figure 29 (plate 2) shows a comparison of the experimental advection patterns. In this case a higher value of θ is chosen so that large-scale structures develop in only a few periods. The agreement between the sine wave and the sawtooth wave is quite satisfactory and the square wave produces a qualitatively similar picture. However, the dye area coverage for the square wave is larger than the other waveforms. An explanation for this is that the contribution of the higher-order harmonics in the Fourier series is appreciable for the square waveform. The coefficients of the higher-order harmonics for the sine wave are zero and for the sawtooth wave they are an order-of-magnitude less than the leading term. This explains the close matching between the sine and sawtooth waveforms. However, the second term of the square waveform is only a factor of 2 less than the first term, and for a system with such a large perturbation ($\epsilon = O(1)$) produces a somewhat larger effect. The conclusion is that any choice, for an experiment or computation, of a (nearly) single-frequency forcing function produces the same qualitative results.

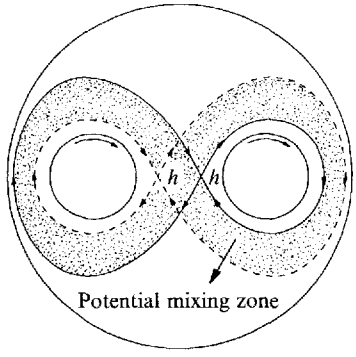

FIGURE 30. Potential mixing zone for the vortex mixing flow; $R_o/R_i = 4.0$, $e = 0.67$. Dashed line denotes $r = 1/5$ and solid lines denote $r = 5.0$.

6. Slow mixing

Very slow variations of a control parameter can dramatically localize mixing patterns. Kaper & Wiggins (1993) have extended the technique of adiabatic invariance to calculate these effects for an eccentric cylinder flow when the speed ratio of the cylinders oscillates very slowly. They find that mixing is confined to smeared out bands centred on homoclinic orbits called 'potential mixing zones'; they also find, as the period of variation shortens, an abrupt transition from adiabatic to non-adiabatic behaviour. In this section we experimentally verify the existence of potential mixing zones in the VMF under slow variation of the speed ratio of the inner cylinders r. We also investigate the crossover from adiabatic to non-adiabatic forcing and the breakout from potential mixing zones. Because its effect is to localize well-mixed regions, it is apparent that adiabatic mixing will not be important to industrial-scale mixing problems; however, in natural systems, e.g. the atmosphere or the oceans, where forcing variations may take place on timescales of seasons or years, this mixing mechanism may be of considerable relevance.

Why should speed matter in Stokes flows? The answer is that adiabatic changes are not merely slow but are quasi-static. An example will make this clearer. Consider the VMF with corotating cylinders in figure 30. The steady flow produces a double homoclinic loop. When $r > 1$, the central hyperbolic point h moves on the x-axis right of centre and the homoclinic orbits are the solid lines in figure 30. When $r < 1$, h moves left of centre and the homoclinic orbits are the dashed lines. If r oscillates about 1 as

$$r = [1 + \epsilon \sin(2\pi t/T)]/[1 - \epsilon \sin(2\pi t/T)], \tag{33}$$

the orbits oscillate between the solid and dashed lines in figure 30. An adiabatic change in r is then one in which the oscillation period T is large and remains nearly constant as fluid particles make circuits around the loops and experience effectively no change in the instantaneous streamline patterns. However, the instantaneous streamlines do change slowly and fluid particles veer away from their initial paths at very small angles. The separation of the manifolds is very small, and the experimentally observed lobes generated by this quasi-static time-dependence are very thin and cling to the unperturbed orbit. Kaper & Wiggins (1993) showed that the transport and mixing for adiabatic forcing is confined to the area swept out between the extremes of the changing homoclinic loops, for instance the shaded area in figure 30.

In the experiments to investigate potential mixing zones in complex flows and the crossover from adiabatic to non-adiabatic forcing, the inner cylinders rotate in a sine waveform (see (31)) with $\epsilon = 8/\pi^2$. The maximum and minimum speed ratios of the

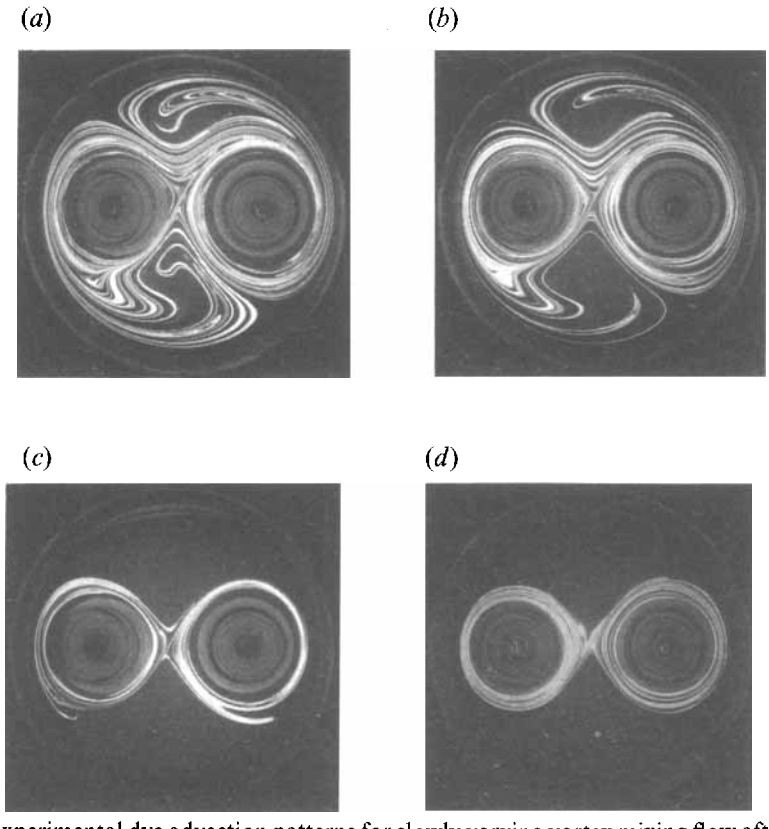

FIGURE 31. Experimental dye advection patterns for slowly varying vortex mixing flow after 5 periods; $R_o/R_i = 4$, $e = 0.67$, $\theta = 2880°$, and corotating cylinder motion. Cylinders move in a sine wave (see (31)) with $\epsilon = 8/\pi^2$: (*a*) $T = 100$ s, (*b*) $T = 125$ s, (*c*) $T = 175$ s, (*d*) $T = 250$ s.

cylinders are $r = 8.32$ and $r = 0.12$ and the range of r is such that no flow bifurcations occur (figure 9). The oscillation period T ranges from 100 to 250 s. It can happen for the longest experimental runs (several hours or so) that molecular diffusion of the dye noticeably blurs the experimental picture. Blurring by diffusion would be very difficult to separate in these experiments from the adiabatic broadening into mixing zones. In our experiments, though, adiabatic effects appear well before dye diffusion becomes noticeable and diffusion plays no role in the data shown in figures 31 and 32.

Figure 31 shows the dye advection patterns in the VMF at four different time periods of oscillation. The angular displacements per period θ of the cylinders in all cases are the same and each pattern in figure 31 corresponds to the same total angular displacement of the cylinders. The pattern in figure 31 (*a*) corresponds to relatively fast oscillation as studied in §4, and dye spreads by the action of unstable manifolds moving wildly in space. As the period increases, the unstable manifolds align with the homoclinic loops of the instantaneous streamline portraits and dye does not spread beyond the region swept by these homoclinic loops. It is worth noting that the mixing pattern in figure 31 (*d*) is of the shape as the potential mixing zone in figure 30.

A digitization of sequences of pictures similar to those in figure 31 allows the calculation of fractional area coverage α, which in turn may be used to characterize the transition from adiabatic to non-adiabatic forcing. Figure 32 shows α versus $1/T$ for constant $St = 0.04$. There are two distinct regions in the graph. At low frequencies α is nearly constant as the dye is confined to the potential mixing zone, which seems to

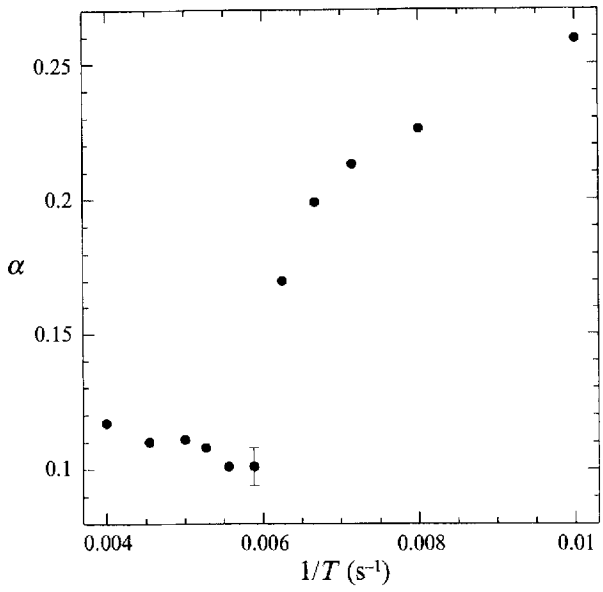

FIGURE 32. Fractional area coverage *vs.* $1/T$ for the vortex mixing flow showing the transition from adiabatic to non-adiabatic behaviour. The error bar indicates the experimental run-to-run variability in the area coverage. Corotating cylinder motion, protocol A, $\theta = 2880°$, $e = 0.670$, $R_o/R_i = 4$.

be of nearly constant size. At higher frequencies dye escapes the potential mixing zone to mix in the rest of the VMF domain. The error bar in the figure indicates the run-to-run variability due to small variations in the initial dye placement and amount of dye used; the accuracy of an individual area measurement is about half that of the error shown. The transition frequency is very sharp, suggesting the existence of a critical manifold angle separating the slow and fast regimes.

7. A complex test problem: optimum mixing conditions for the VMF

In spite of all the recent advances in the characterization of chaotic advection there is still no optimum recipe to characterize and rank the mixing abilities of arbitrarily chosen flows. A measure of the difficulties in achieving such an objective are highlighted by means of a test case. The problem selected is to find the optimum eccentricity – all parameters other than e are held constant – giving the 'best' mixing in the VMF. By best mixing we mean the existence of the thinnest possible striations distributed uniformly over the domain. In general a well-mixed system corresponds to maximizing the average stretching and minimizing the standard deviation (Muzzio *et al.* 1991). A superficial analysis might suggest the use of one of the tools in §4 as a merit function to find the optimum e. However, the limitations of each tool, either failing at larger perturbations or being not feasible to compute, disqualify every dynamical tool considered in this paper from assuming the role of a 'perfect' merit function in a traditional optimization sense. Melnikov calculations of lobe area come closest to being useful as a merit function and in fact, do fulfil that role up to perturbations where the method breaks down. Unfortunately, better mixing is almost always found at larger perturbations. Nevertheless, since the Melnikov method is computationally least expensive, we go through a Melnikov example below. To uncover a truer approximation to the optimum, however, we then use a larger perturbation and apply the dynamical tools in a sequence to 'sieve' away most of

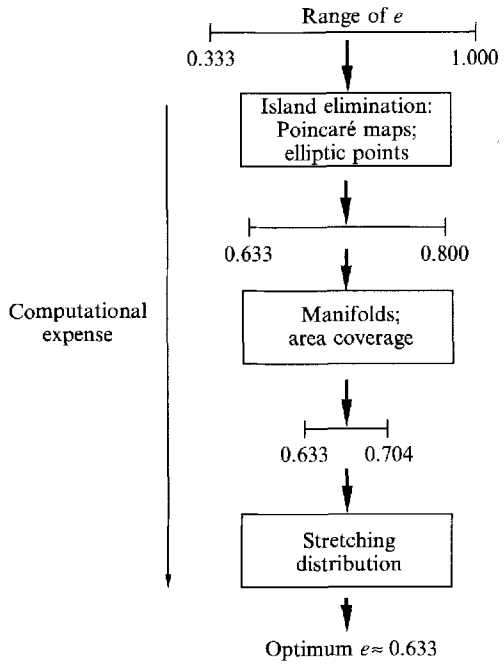

FIGURE 33. Schematic of a 'dynamical sieve' used to search parameter space and find the optimum eccentricity for the vortex mixing flow through successive application of different dynamical tools. The computational expense increases (faster than linearly) for successive refinement of the optimum parameter range. The definition of a good mixing process changes at each level. Island elimination uses Poincaré maps and elliptic periodic points to order 3 to remove non-mixing regions. Area coverage uses the extent of the unstable manifolds of periodic hyperbolic points to order 3 to remove mixing confinement. Stretching distributions indicate which parameter value for equal area coverage, gives the smallest fraction of thick striations.

parameter space, leaving an approximate global optimum. Figure 33 summarizes the steps in the dynamical sieve, which are arranged in order of computational expense. The diagram has the look of an inverted pyramid with its tip pointing to the optimum value of e. At every level of the pyramid the definition of a good mixing process changes with the tool used to move from one level to the next. Companion experiments verify the results at each level of the pyramid. Removal of parameter space stops when experiments are no longer able to distinguish one value of e from another.

The operating parameters for the VMF test problem are $r = 1$, corotating cylinders, and protocol A. These parameters are kept fixed as an optimum e is sought. A perturbation angle of $\theta = 360°$ is small enough to allow use of the Melnikov method described in §4.4. In the range $0.333 < e \leqslant 0.704$, the unperturbed VMF with corotating inner cylinders exhibits double homoclinic loops emanating from the central hyperbolic critical point that enclose the inner cylinders and two heteroclinic loops emanating from the parabolic points on the outer cylinder, as shown in figure 8(a, b). At $e = \frac{1}{3}$ the inner cylinders touch each other; this is a singular case for the BIEM and the flow cannot be solved. For $e > 0.704$, double homoclinic loops do not enclose the inner cylinders and are much smaller in size (figure 8c). Intuitively, in such cases, chaos will be localized; therefore, in calculating the lobe area using the Melnikov method we concentrate on the range $0.333 < e < 0.704$ and evaluate the N_i terms in (28) for both the heteroclinic and homoclinic orbits. In all cases the term N_1 is at least an order-of-magnitude larger than the other terms, so the lobe area μ is given largely

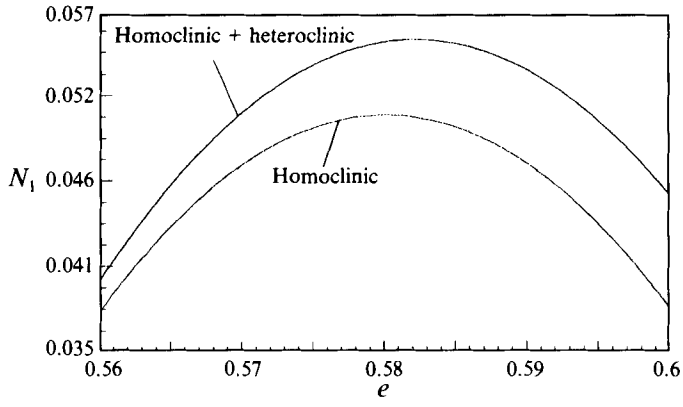

FIGURE 34. Lobe area from the Melnikov method for $\theta = 360°$, $R_o/R_i = 4$, sine wave, and corotating cylinder motion. The optimum eccentricity calculated using the sum of N_1 values of both heteroclinic and homoclinic orbits lies at $e = 0.582$.

by N_1. Figure 34 shows a plot of N_1 for the homoclinic orbit and the sum of N_1 values for both the heteroclinic and homoclinic orbits as a function of e. The N_1 values for the homoclinic orbits show a maximum at $e = 0.580$ and that of the heteroclinic and homoclinic orbits together show a maximum at $e = 0.582$. The heteroclinic loops gradually dip towards the hyperbolic point with increase in e and when perturbed gradually increase the degree of chaos. This is reflected in the gradual increase in the values of N_1 for the heteroclinic orbit with e. However, the N_1 values for the heteroclinic orbits are much smaller than those for the homoclinic orbits and change the optimum only slightly. The optimum value of e obtained from the Melnikov method is valid for only small perturbations. However, at small perturbations chaos is confined to the neighbourhood of the homoclinic loops of the unperturbed system and the global mixing is poor. Therefore, we must operate at larger perturbations and use the other tools at our disposal to search for a true optimum.

To continue the test problem, a perturbation value of $\theta = 1440°$ is chosen because for these parameters and with $e = 0.670$ we have previously observed global chaos. The existence of islands indicates poor mixing. Therefore, we consider island elimination as the first step to finding an optimum. Larger islands are visually apparent in Poincaré sections and smaller islands are determined by finding the elliptic periodic points. Figure 35 shows the Poincaré sections for various eccentricities. If the Poincaré section, which is an indicator of asymptotic structure, shows regular regions or islands, the short-time dye advection pattern of the same flow will show even larger islands. Thus, at this stage we can eliminate values of e that generate regular regions. From figure 35 the optimum lies in the range $0.530 < e < 0.930$. Next, we search for elliptic periodic points. After finding the elliptic points up to P-3, the range for the optimum is further narrowed to $0.633 \leqslant e \leqslant 0.800$.

Parameter values that mix well spread dye over a large portion of the domain. Once islands are eliminated, we use area coverage comparisons to proceed. Calculation of manifold extent is the chief tool. As shown in figure 35, Poincaré sections for $e = 0.670$ and $e = 0.800$ look equally chaotic. However, in order to determine which mixes better, we look for hyperbolic periodic points up to P-3 for both flows and calculate their manifolds. From the case $e = 0.800$, the manifolds of all periodic points are localized (see figure 23), so that even though stretching is high along the manifolds, the global mixing is poor. Similar circumstances apply to all flows with double homoclinic loops

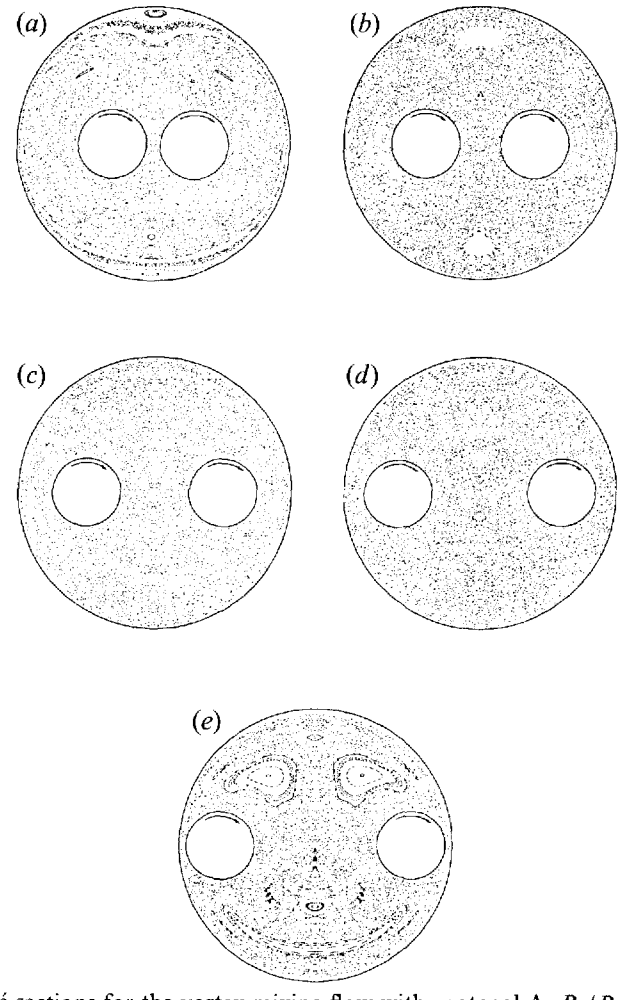

FIGURE 35. Poincaré sections for the vortex mixing flow with protocol A, $R_o/R_i = 4$, and $\theta = 1440°$ as a function of eccentricity: (*a*) = 0.40, (*b*) $e = 0.53$, (*c*) $e = 0.67$, (*d*) $e = 0.80$, (*e*) $e = 0.93$, which has given this flow the nickname 'smiley-face flow'.

not enclosing the inner cylinders in their unperturbed flow, which happens at a flow bifurcation for $e > 0.704$ (figure 7). Next we perform experiments to see if the advection patterns reveal any information about a true optimum. In figure 36(*a*, *b*), identical initial conditions are used in the form of a straight line of dye injected along the *y*-axis. Also shown in figure 36(*c*, *d*) are the dye advection patterns for $e = 0.766$ and $e = 0.930$. Flow bifurcations have occurred for these latter two eccentricities and in both of them unperturbed homoclinic loops do not enclose the inner cylinders (see figure 7). Therefore, it is evident that mixing in the range $e > 0.704$ is poor. Thus, the range of e containing an optimum is further reduced to $0.633 \leqslant e \leqslant 0.704$.

Further refinement within the range $0.633 \leqslant e \leqslant 0.704$ is more difficult. The flows do not have any elliptic periodic points and calculating the manifold structures of the hyperbolic periodic points is not helpful at this stage for two reasons. (i) Flows at some values of e in the range possess a large number of periodic points even if only the periodic points up to P-3 are included. For example the $e = 0.704$ case has an array of hyperbolic points: 27 P-3 points, two P-2 points, and three P-1 points. (ii) In this range

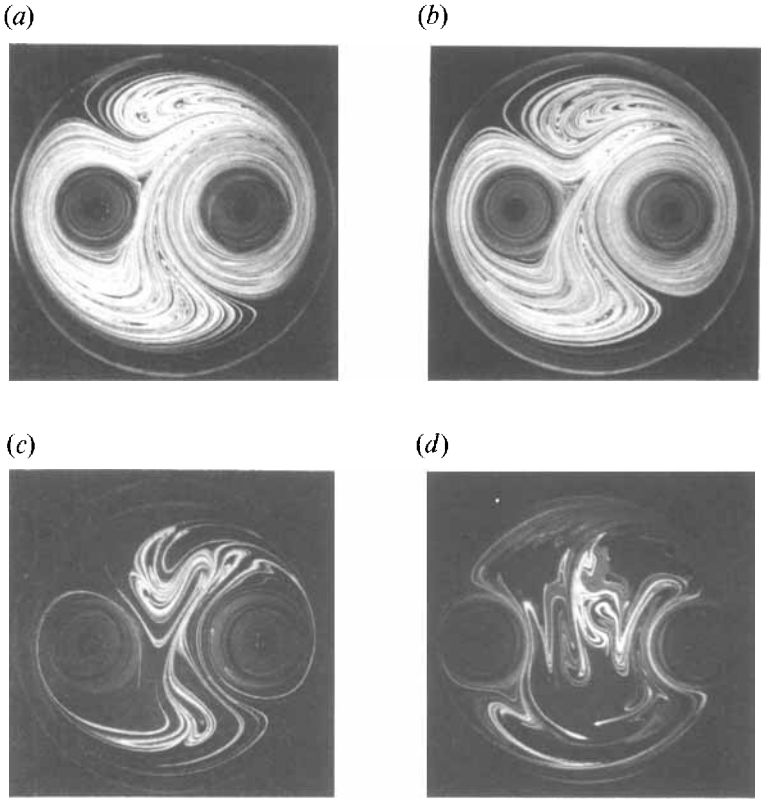

FIGURE 36. Dye advection experiments with different eccentricities; protocol A, $\theta = 1440°$, and $R_o/R_i = 4$. (*a*) $e = 0.670$ after 6 periods, (*b*) $e = 0.704$ after 6 periods, (*c*) $e = 0.766$ after 8 periods, (*d*) $e = 0.930$ after 15 periods.

of eccentricities cumulative stretching along manifolds is of the same order and the manifold structures look similar. Figure 36(*a*, *b*) shows dye advection experiments for $e = 0.670$ and 0.704 respectively. The dye advection patterns are quite similar. Is it worth continuing? If experiments cannot distinguish between parameters, then perhaps, as far as an optimization problem goes, we have for all practical purposes finished. Let us look a little closer. Figure 37(*a*, *c*) is a digitized versions of figure 36(*a*, *b*) with the dyed area shown in black. If we calculate the fractional area coverage α, we find that both figures have $\alpha = 0.77$, verifying the visual conclusion of equal area coverage. However, the thickest striations of a pattern contain the most dye and so are the brightest. Figure 37(*b*, *d*) repeats 37(*a*, *c*) but shows only the brightest quarter of the pixels. Now a clear distinction between the patterns emerges. Figure 37(*b*) at $e = 0.670$ has 1.6% of its area covered by bright/thick striations, mostly falling at the tips of folds, which are expected to be places of low stretching. In contrast figure 37(*d*) at $e = 0.704$ has 20% of its area covered by bright/thick striations. Quantitative image analysis has not been used extensively yet to analyse mixing patterns, and we are not able as yet to extract a full-blown striation distribution from a well-mixed pattern to make detailed comparisons with stretching calculations, though image analysis of experiments is clearly able to qualitatively distinguish different stretching distributions. Therefore, it may be deemed worthwhile for this problem to calculate stretching distributions (the most expensive tool – by three orders of magnitude – discussed in §4) for $0.633 \leqslant e \leqslant 0.704$ to further narrow the optimum eccentricity range.

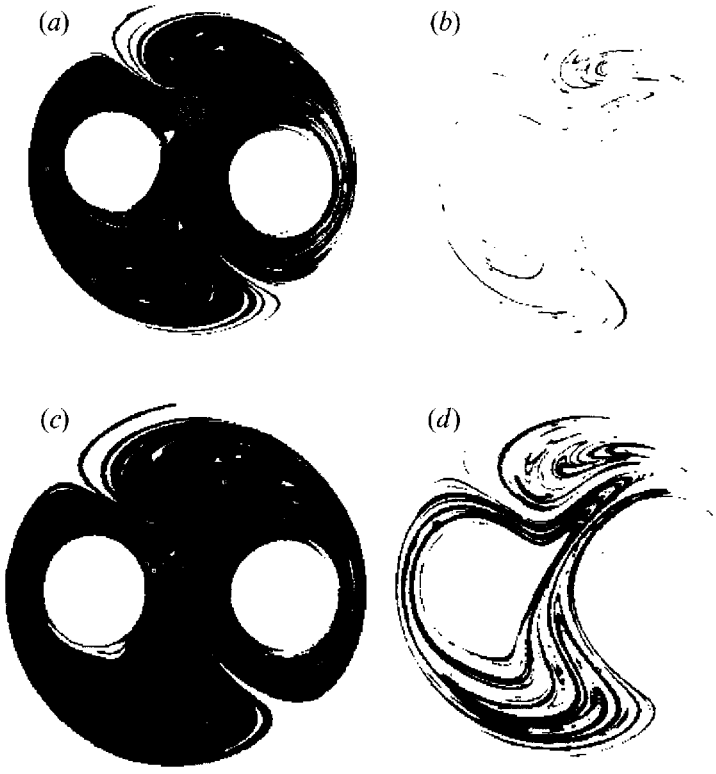

FIGURE 37. Digitized images of advection experiments for the vortex mixing flow in figure 36(*a*, *b*): (*a*, *c*) total area coverage in 6 periods, (*b*, *d*) area coverage by the brightest quarter of pixels showing the thick striations. (*a*, *b*) $e = 0.670$; (*c*, *d*) $e = 0.704$.

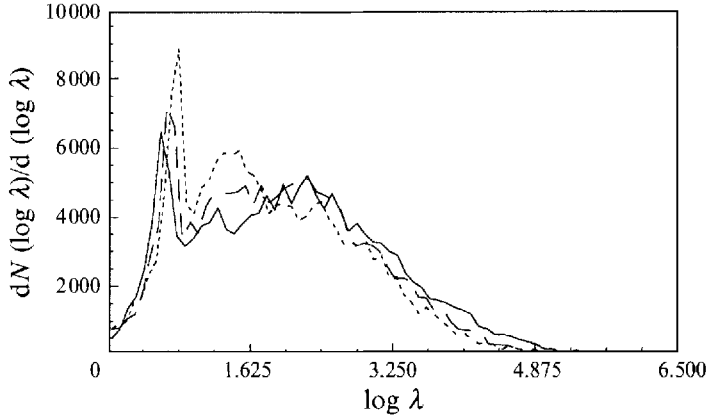

FIGURE 38. Distribution of stretching values for the vortex mixing flow; $R_o/R_i = 4$, $\theta = 1440°$, protocol A, and corotating cylinder motion. $dN(\log\lambda)$ represents the number of particles between $\log\lambda$ and $\log\lambda + d\log\lambda$. ····, $e = 0.633$; ——, $e = 0.67$, – – –, $e = 0.704$.

To compute a distribution of stretching values we uniformly distribute ~ 15000 points in the flow domain and compute λ at each point using equations (15) and (16). A plot of the stretching distribution is prepared following the methods of Muzzio *et al.* (1991). Figure 38 shows the stretching distribution for $e = 0.633$, 0.670, and 0.704 after three periods. The distributions are bimodal with a sharp peak in the low stretching range which increases with increasing e. This implies that a larger number of points

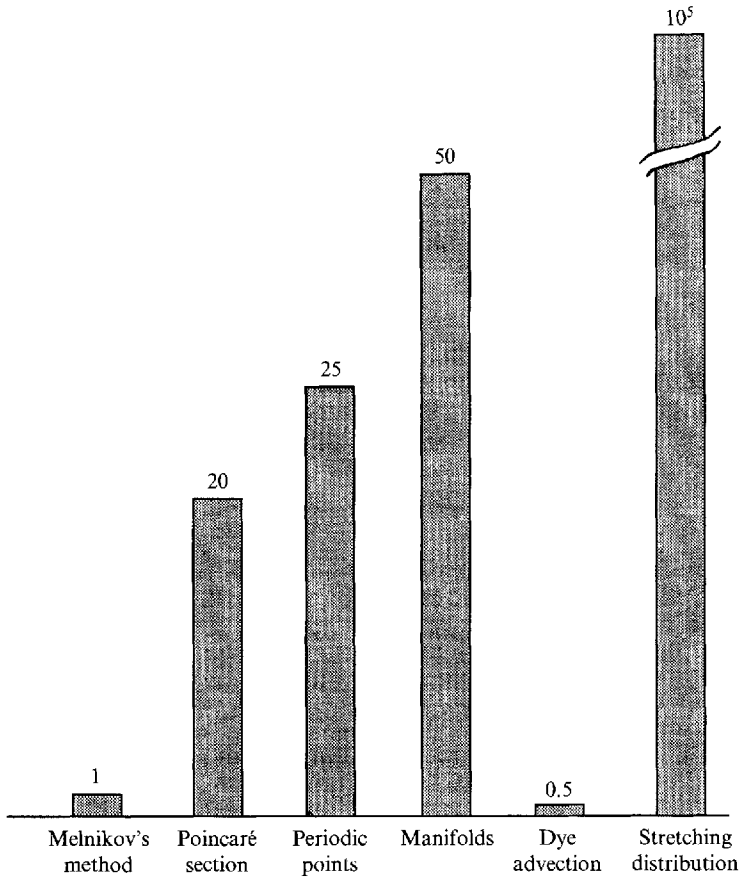

FIGURE 39. Relative timing graph for dynamical tools with computational times scaled by that for the Melnikov method. Note the unequal scale for stretching distributions. For the vortex mixing flow a typical calculation of lobe areas using the Melnikov method takes approximately 10 CPU minutes on an SGI-R4000 workstation.

experience small stretching in the $e = 0.704$ case than in the $e = 0.670$ or $e = 0.633$ cases. Calculating the percentage of particles with $\lambda \geqslant 100$ we find that $e = 0.633$ has 81%; $e = 0.670$ has 79%; and $e = 0.704$ has 66%. This is in qualitative agreement with figure 37 in that $e = 0.704$ has the larger fraction of thick striations. This places the optimum eccentricity close to $e = 0.633$. However, one should note that the calculation of stretching distributions is much costlier than the calculation of area coverage from experimental advection patterns (figure 39) and any information anticipated from knowledge of a stretching distribution should be carefully weighed against the time costs. We note that these extreme costs could in principle be considerably reduced because stretching distribution calculations are eminently suitable for parallelization.

To summarize the relative merits of the dynamical tools used in this problem, we note several important points: (i) a Poincaré section of a flow may look globally chaotic but it should not be trusted to give the short-time mixing behaviour of the flow because the Poincaré section does not contain any rate information; (ii) stretching along manifolds does not correlate with a dispersed global mixing pattern. Two flows may differ appreciably in the amount of stretching along manifolds but the flow with manifolds distributed throughout the space is the better mixing flow, e.g. $e = 0.670$

exhibits much better mixing than $e = 0.800$; (iii) stretching distributions are very expensive yet may not be highly discriminating, e.g. there is just a 2% difference between $e = 0.633$ and 0.670. Also stretching distribution functions are not entirely straightforward to interpret and more work seems necessary in this regard. We may, however, note that improvement in quantitative image analysis techniques will probably make experiments more attractive in practical situations than calculating stretching distributions.

8. Conclusions

Comparative experimental and computational studies conducted on two new flows – a vortex mixing flow and multicell flows in slender cavities – provide a global picture of the virtues and limitations of current dynamical tools, especially as they apply to complex Stokes flows. Experiments and numerical analysis – boundary integral equation methods appears to be ideally suited for this task – show remarkable agreement with each other. This is, however, to be expected, as there are no approximations involved in the simulations. Nevertheless the overlap is not complete. Dye advection experiments, while relatively straightforward experimentally, cannot be really easily duplicated by direct simulations. A knowledge of the way structure builds up in the system – new striations nested within old striations – allows, however, for excellent matching between experiments and computations (see figure 18).

Conclusions, recommendations, and evaluation of the relative merits of techniques are detailed throughout the paper, and here we summarize a few points regarding the state of understanding of chaotic advection in Stokes flows. First, it is apparent that the development of suitable heuristics for the understanding of chaotic flows, even in two-dimensions, is far from complete and several difficulties might be encountered. For example, contrary to commonly accepted wisdom, higher-order periodic points can be more important than period-one points in establishing the advection template and extended regions of large stretching. This is not welcome news as the computation of higher-order periodic points cannot be easily inferred from steady velocity fields. There is good news though. We demonstrate that a broad class of forcing functions – as long as they produce the same displacement per period – produces the same qualitative mixing patterns, and that even though none of the existing dynamical tools alone can successfully fulfil the role of a merit function, the collection of currently available tools can be applied successively as a dynamical sieve to uncover a global optimum. A detailed example provides a ranking through the cost per step associated with each tool (see figure 39).

How should a new flow be analysed? A few recommendations can be made. The first issue is to try to qualitatively predict the correct streamline pattern without resorting to the expense of exact computation. Intuition based on experience is invaluable in this regard but topological relations constraining the number of physically realizable choices are extremely useful as well. A computation yielding boundary vorticity, and hence the location of parabolic points, is in general enough to infer the entire velocity field. If the object is to mix, it should be remembered that the mixing behaviour of the flow is dictated by the amount of streamline crossing and this in turn depends strongly on the flows's position in the bifurcation diagram as the forcing is changed. However, crossing alone does not guarantee rapid mixing. Flow regions confined by streamlines anchored to parabolic points are typically associated with low circulation rates and compartmentalized mixing.

The second issue to consider is both the symmetries of the flow and the symmetries

of the forcing protocol. The observation phase is critical. If the observation phase is chosen poorly, flow symmetries are hidden, and analysis becomes needlessly complicated. Symmetries should be exploited to reduce computational workloads. In this regard it is important to remember that while Poincaré maps provide the least expensive asymptotic picture of the global behaviour of a flow and a rough estimate of mixing characteristics and how they change with different protocols and parameter values, they can also lead to substantial errors when trying to anticipate results of short-time dye advection experiments. Poincaré sections always err on the conservative side: regular regions in Poincaré plots appear as even larger islands in dye advection experiments; if Poincaré sections do not exhibit any regular regions, one cannot conclude that the flow mixes globally, because particle paths may appear regular for many periods, taking on the 'look' of chaotic motion only after hundreds or even thousands of periods of motion.

The next issue to consider is low-order periodic points and their associated manifolds. Techniques to compute them accurately have been provided and manifolds can be computed accurately for about 10–15 periods. It is wise to compare the stretching values along the unstable manifolds rather than comparing just the eigenvalues of the periodic points. High stretching rates are important for rapid mixing. Stretching rates, unfortunately, do not always indicate the extent to which manifolds will be distributed throughout the flow region; manifolds with high rates of stretching might in fact be confined to relatively restricted regions.

Finally, the unstable manifolds must be calculated for a reasonable number of periods as to allow for interaction with other periodic points since this is what in fact controls the transport. The Melnikov method and adiabatic techniques are potentially very useful but care should be taken that conditions for applicability are valid on analytical and experimental ends. Stretching distributions, while providing a wealth of information, should be used sparingly. They are extremely expensive and often hard to interpret. It is likely that improvement in quantitative image analysis techniques will make direct experiments more attractive in practical situations than calculating stretching distributions.

All our examples involve bounded flows driven by boundary motions without change of geometry, i.e. boundaries moving tangentially to themselves. A second class of bounded flows might involve area-preserving time-periodic changes of geometries (e.g. boundaries displaced normal to themselves (Jana, Tjahjadi & Ottino 1994)). This class of flows requires more computational expense but, except for this issue, many of our observations can be extended without modification to flows involving changes of geometry as well. Open flows, such as those involving backward step flows or flows induced by passing a flow over a wedge or a cavity involve several issues not accounted for in this presentation, even though several of the ideas presented here might be valuable in this regard.

This work was supported by the Department of Energy, Basic Energy Sciences.

Appendix A. boundary integral equation methods

The Stokes equations along with the equation of continuity form a set of partial differential equations which may be transformed into integral equations in terms of the boundary velocities and the strength of unknown point forces or point dipoles distributed along the boundaries. The integral equations have the advantage of reduced dimensionality: a two-dimensional flow can be studied in terms of line

integrals. A set of linear algebraic equations results upon discretization of the integral equations which are solved by direct or iterative methods to obtain the strength of the point forces or dipoles. The velocity field at any interior point is then obtained analytically from these point forces or dipoles without any need for interpolation.

The VMF is solved using the single-layer formulation of BIEM. The usefulness of alternative formulations, for example the double-layer formulation, is discussed in detail in Kim & Karilla (1991) and Pozrikidis (1992). Following Higdon (1985) the integral equations can be written as

$$u_i(\boldsymbol{x}_0) = C \int_S (S_{ij}(\boldsymbol{x}-\boldsymbol{x}_0) f_j(\boldsymbol{x}) - T_{ijk}(\boldsymbol{x}-\boldsymbol{x}_0)\, u_j(\boldsymbol{x})\, n_k)\, \mathrm{d}S; \quad i,j,k = 1,2, \tag{A 1}$$

where u_i is the ith component of the velocity, f_j is the jth component of the point force, $\boldsymbol{x}_0$ is a *field point* or a point inside the fluid, $\boldsymbol{x}$ is a point on the boundary, $\boldsymbol{n}$ is the normal to the boundary pointing out of the fluid, and n_k is its kth component. S is the boundary of the domain and

$$S_{ij}(\hat{\boldsymbol{x}}) = \delta_{ij} \ln r - \hat{x}_i \hat{x}_j / r^2 \tag{A 2}$$

is the free-space Green's function, where $\hat{\boldsymbol{x}} = \boldsymbol{x}-\boldsymbol{x}_0$, $r = |\hat{\boldsymbol{x}}|$, and T_{ijk} is the stress tensor associated with the Green's function. The factor C in (A 1) is $1/4\pi\mu$ when the point $\boldsymbol{x}_0$ is inside the fluid and $1/2\pi\mu$ when the point $\boldsymbol{x}_0$ is on the boundary of the domain; μ here is the shear viscosity of the fluid.

In this work, the boundary of the flow domain is discretized using straight line segments and the values of $\boldsymbol{u}$ and $\boldsymbol{f}$ are taken to be piecewise constant along each segment. The discretized form of (A 1) is

$$u_i(\boldsymbol{x}_m) = \sum_{n=1}^{N} A_{ij}(\boldsymbol{x}_m, \boldsymbol{x}_n) f_j(\boldsymbol{x}_n) + \sum_{n=1}^{N} B_{ij}(\boldsymbol{x}_m, \boldsymbol{x}_n)\, u_j(\boldsymbol{x}_n), \tag{A 3}$$

where $\boldsymbol{x}_m$ is a point in the flow and $\boldsymbol{x}_n$ is the discrete boundary point at the middle of segment n. The expressions for A_{ij} and B_{ij} are

$$A_{ij}(\boldsymbol{x}_m, \boldsymbol{x}_n) = C \int_{-\delta_n/2}^{\delta_n/2} S_{ij}(\boldsymbol{x}_m - \boldsymbol{x}_n - \xi \boldsymbol{t}_n)\, \mathrm{d}\xi, \tag{A 4a}$$

$$B_{ij}(\boldsymbol{x}_m, \boldsymbol{x}_n) = -C \int_{-\delta_n/2}^{\delta_n/2} T_{ijk}(\boldsymbol{x}_m - \boldsymbol{x}_n - \xi \boldsymbol{t}_n)\, n_k\, \mathrm{d}\xi, \tag{A 4b}$$

where δ_n is the length of the nth boundary segment, $\boldsymbol{t}$ and $\boldsymbol{n}$ are unit tangent and normal vectors to the nth segment, and ξ is the local spatial variable. Estimates of the error due to discretization of the integral equation and piecewise smooth approximations of $\boldsymbol{u}$ and $\boldsymbol{f}$ along the segments are discussed in Higdon (1985) and Pozrikidis (1992).

The terms A_{ij} and B_{ij} are evaluated using numerical quadrature. Considering the point $\boldsymbol{x}_m$ on the boundary, the system of equations (A 3) are solved using LU-decomposition to obtain the strength of the point force $\boldsymbol{f}$. Once $\boldsymbol{f}$ is obtained, the velocity at any interior point is calculated from (A 3) considering the point $\boldsymbol{x}_m$ inside the fluid.

Appendix B. Symmetry relations of flow $F_B F_A$ with corotating cylinder motion

The mapping of a point $\boldsymbol{x}_n$ under flow $F_B F_A$ using protocol PA and co-rotating cylinder motion can be written as

$$\boldsymbol{x}_{n+1} = \boldsymbol{M} \boldsymbol{x}_n, \tag{B 1}$$

where $\boldsymbol{M} = \boldsymbol{F}_B \boldsymbol{F}_A$, where $\boldsymbol{F}_A$ and $\boldsymbol{F}_B$ are the mappings described by flows A and B respectively. In mapping $\boldsymbol{M}$, flow A is applied first followed by flow B. Exploiting the symmetry relations of table 1,

$$\boldsymbol{M} = \boldsymbol{F}_B \boldsymbol{F}_A = \boldsymbol{S}_y \boldsymbol{F}_A^{-1} \boldsymbol{S}_y \boldsymbol{S}_y \boldsymbol{F}_B^{-1} \boldsymbol{S}_y = \boldsymbol{S}_y \boldsymbol{F}_A^{-1} \boldsymbol{F}_B^{-1} \boldsymbol{S}_y = \boldsymbol{S}_y (\boldsymbol{F}_B \boldsymbol{F}_A)^{-1} \boldsymbol{S}_y, \tag{B 2}$$

where $\boldsymbol{S}_y \boldsymbol{S}_y = \boldsymbol{1}$. So the mapping $\boldsymbol{M}$ has a time-reversal reflectional symmetry about the y-axis and its fixed line of symmetry is the y-axis. Another symmetry can be derived in a similar fashion by using the self-symmetry relations given in table 1:

$$\boldsymbol{M} = \boldsymbol{F}_B \boldsymbol{F}_A = \boldsymbol{S}_x \boldsymbol{F}_B^{-1} \boldsymbol{S}_x \boldsymbol{S}_x \boldsymbol{F}_A^{-1} \boldsymbol{S}_x = \boldsymbol{S}_x \boldsymbol{F}_B^{-1} \boldsymbol{F}_A^{-1} \boldsymbol{S}_x = \boldsymbol{S} (\boldsymbol{F}_B \boldsymbol{F}_A)^{-1} \boldsymbol{S}^{-1}, \tag{B 3}$$

where $\boldsymbol{S}_x \boldsymbol{S}_x = \boldsymbol{1}$ and $\boldsymbol{S} = \boldsymbol{F}_B \boldsymbol{S}_x$. So the flow has a non-trivial symmetry, $\boldsymbol{S} = \boldsymbol{F}_B \boldsymbol{S}_x$ and the *fixed line* of this symmetry or *symmetry line* $\{\boldsymbol{X}\}$ is obtained by solving

$$\boldsymbol{S}\{\boldsymbol{X}\} = \{\boldsymbol{X}\}. \tag{B 4}$$

It can be easily shown that the solution of (B 4) is $\{\boldsymbol{X}\} = \boldsymbol{F}_B^{\frac{1}{2}}\{\boldsymbol{x}\}$, i.e. the symmetry line $\{\boldsymbol{X}\}$ is a curved line obtained by advecting the x-axis by $\boldsymbol{F}_B^{\frac{1}{2}}$.

REFERENCES

AREF, H. 1984 Stirring by chaotic advection. *J. Fluid Mech.* **143**, 1–21.

AREF, H. 1991 Chaotic advection of fluid particles. *Phil. Trans. R. Soc. Lond.* A **333**, 273–281.

BALLAL, B. Y. & RIVLIN, R. S. 1976 Flow of a Newtonian fluid between eccentric rotating cylinders: inertial effects. *Arch. Rat. Mech. Anal.* **62**, 237–294.

BEIGE, D., LEONARD, A. & WIGGINS, S. 1991 Chaotic transport in the homoclinic and heteroclinic tangle regions of quasiperiodically forced two-dimensional dynamical systems. *Nonlinearity* **4**, 775–819.

BURGGRAF, O. R. 1966 Analytical and numerical studies of the structure of steady separated flows. *J. Fluid Mech.* **24**, 113–151.

CAMASSA, R. & WIGGINS, S. 1991 Chaotic advection in Rayleigh–Bénard flow. *Phys. Rev.* A **43**, 774–797.

CHAIKEN, J., CHEVRAY, R., TABOR, M. & TAN, Q. M. 1986 Experimental study of Lagrangian turbulence in a Stokes flow. *Proc. R. Soc. Lond.* A **408**, 165–174.

CHIEN, W.-L., RISING, H. & OTTINO, J. M. 1986 Laminar mixing and chaotic mixing in several cavity flows. *J. Fluid Mech.* **170**, 355–377.

FLEGG, H. G. 1974 *From Geometry to Topology*. The English University Press Ltd.

FRANJIONE, J. G., LEONG, C.-W. & OTTINO, J. M. 1989 Symmetries within chaos: a route to effective mixing. *Phys. Fluids* A **1**, 1772–1783.

FRANJIONE, J. G. & OTTINO, J. M. 1992 Symmetry concepts for geometric analysis of mixing flows. *Phil. Trans. R. Soc. Lond.* A **338**, 301–323.

GUCKENHEIMER, J. & HOLMES, P. 1983 *Nonlinear Oscillations, Dynamical Systems, and Bifurcations of Vector Field*. Springer.

HIGDON, J. J. L. 1985 Stokes flow in arbitrary two-dimensional domains: shear flow over ridges and cavities. *J. Fluid Mech.* **159**, 194–226.

HOBSON, D. 1993 An efficient method for computing invariant manifolds of planar maps. *J. Comput. Phys.* **104**, 14–22.

JANA, S. C. & OTTINO, J. M. 1992 Chaos-enhanced transport in cellular flows. *Phil. Trans. R. Soc. Lond.* A **338**, 519–532.

JANA, S. C., TJAHJADI, M. & OTTINO, J. M. 1994 Chaotic mixing of viscous fluids by periodic changes in geometry: the baffled cavity flow. *AIChE J.* (to appear).

JEFFREY, D. J. & SHERWOOD, J. D. 1980 Streamline patterns and eddies in low-Reynolds-number flow. *J. Fluid Mech.* **96**, 315–334.

KAPER, T. J. & WIGGINS, S. 1993 An analytical study of transport in Stokes flows exhibiting large-scale chaos in the eccentric journal bearing. *J. Fluid Mech.* **253**, 211–243.

KIM, S. & KARILLA, S. J. 1991 *Microhydrodynamics: Principles and Selected Applications.* Butterworth–Heinemann.

KUSCH, H. A. & OTTINO, J. M. 1992 Experiments on mixing in continuous flows. *J. Fluid Mech.* **236**, 319–348.

LEONG, C. W. 1990 Chaotic mixing of viscous fluids in time-periodic cavity flows. PhD thesis, University of Massachusetts at Amherst.

LEONG, C. W. & OTTINO, J. M. 1989*a* Experiments on mixing due to chaotic advection in a cavity. *J. Fluid Mech.* **209**, 463–499.

LEONG, C. W. & OTTINO, J. M. 1989*b* Gallery of fluid motion. *Phys. Fluids* A **1**, 1441.

LING, F. H. & SCHMIDT, G. 1992 Mixing windows in discontinuous cavity flows. *Phys. Lett.* A **165**, 221–230.

MOFFATT, H. K. 1964 Viscous and resistive eddies near a sharp corner. *J. Fluid Mech.* **18**, 1–18.

MUZZIO, F. J., SWANSON, P. D. & OTTINO, J. M. 1991 The statistics of stretching and stirring in chaotic flows. *Phys. Fluids* A **3**, 822–834.

NG, R. C.-Y. 1989 Semi-dilute polymer solutions in strong flows. PhD dissertation, California Institute of Technology.

OTTINO, J. M. 1990 Mixing, chaotic advection, and turbulence. *Ann. Rev. Fluid Mech.* **22**, 207–254.

PAN, F. & ACRIVOS, A. 1967 Steady flows in rectangular cavities. *J. Fluid Mech.* **28**, 643–655.

POZRIKIDIS, C. 1992 *Boundary Integral and Singularity Methods for Linearized Viscous Flow.* Cambridge University Press.

ROM-KEDAR, V., LEONARD, A. & WIGGINS, S. 1990 An analytical study of transport, mixing and chaos in an unsteady vortical flow. *J. Fluid Mech.* **214**, 347–394.

SWANSON, P. D. 1991 Regular and chaotic mixing of viscous fluids in eccentric rotating cylinders. PhD dissertation, University of Massachusetts at Amherst.

SWANSON, P. D. & OTTINO, J. M. 1990 A comparative computational and experimental study of chaotic mixing of viscous fluids. *J. Fluid Mech.* **213**, 227–249.

WANNIER, G. H. 1950 A contribution to the hydrodynamics of lubrication. *Q. Appl. Maths.* **VIII**, 1–32.

WIGGINS, S. 1988 *Global Bifurcations and Chaos.* Springer.

WIGGINS, S. 1992 *Chaotic Transport in Dynamical Systems.* Springer.